RESEARCH ARTICLE

ADVANCED HEALTHCARE MATERIALS
www.advhealthmat.de

A Novel Injectable Composite Hydrogel HAp-GelMA Co-Doped Magnesium/Zinc Promotes Bone Generation and Angiogenesis Synergistically

Lei Qiang, Tianyou Zhang, Quan Zhang, Ting Yang, Jing Shan, Guanlu Shen, Weize Kong, Jing Wei, Jinwu Wang, Yihao Liu, Haoyi Niu,* and Pengfei Zheng**

Bone is a crucial organ in the human body; however, conventional bone repair materials, such as autologous and allogeneic bone, are associated with challenges like limited availability and infection risks. Therefore, the development of novel biomaterials for bone repair is essential. This study employed a hydrothermal method to synthesize hydroxyapatite (HAp) doped with various elements and characterized its physicochemical properties. These findings show that the doped HAp particles have a uniform spherical shape and an even distribution of elements. Subsequently, HAp-GelMA composite hydrogels are synthesized, and their mechanical properties and injectability are assessed. The addition of HAp significantly enhanced the stability of the composite hydrogel, making it suitable for the rapid filling of bone defects. In vitro experiments demonstrated that the Zn/Mg dual-doped composite hydrogel effectively promoted cell proliferation and angiogenesis. Furthermore, In vivo studies using a cranial defect model in rats show that the Zn/Mg dual-doped group exhibited significantly better bone regeneration compared to the control group, indicating the material's potential application value in bone tissue engineering and regenerative medicine. In summary, the composite hydrogel scaffold developed in this study shows promising prospects for enhancing angiogenesis and osteogenesis.

1. Introduction

Bone is the fundamental structure of biological organisms, and its integrity is essential for various life activities[1] The bone matrix is composed of ≈70% bioactive hydroxyapatite (HAp), 20% collagen fibers, and 10% water.[2] Bone defects caused by trauma, inflammation, tumors, and osteoporosis are increasingly threatening human health, especially with the aging population, which exacerbates the burden of bone-related diseases. Consequently, bone regeneration and reconstruction present significant clinical challenges.[3] Autologous bone grafting is currently the preferred material for filling or replacing bone defects; however, its limited availability and the need for additional surgery can lead to complications. While Allogeneic bone grafting eliminates the need for a second surgical site and avoids some complications, its unpredictable source increases the risks of disease transmission

L. Qiang, Y. Liu, P. Zheng
Department of Orthopaedic Surgery
Children's Hospital of Nanjing Medical University
Nanjing 210008, P. R. China
E-mail: lyh19950227sjtu@sjtu.edu.cn; zhengpengfei@njmu.edu.cn

T. Yang, H. Niu, P. Zheng
Department of Science and Technology
Children's Hospital of Nanjing Medical University
Nanjing 210008, P. R. China
E-mail: haoyiniu@sjtu.edu.cn

L. Qiang, W. Kong, J. Wang, Y. Liu
Shanghai Key Laboratory of Orthopedic Implant
Department of Orthopedic Surgery Shanghai Ninth People's Hospital
Shanghai Jiao Tong University School of Medicine
Shanghai 200011, P. R. China

Q. Zhang, G. Shen, J. Wei, P. Zheng
Jiangsu Key Laboratory of Marine Bioresources and Environment
Co-Innovation Center of Jiangsu Marine Bio-industry Technology
Jiangsu Key Laboratory of Marine Pharmaceutical Compound Screening
Jiangsu Ocean University
Lianyungang 222005, P. R. China

T. Zhang
The Department of Orthopedics
the First Affiliated Hospital of Nanjing Medical University
Nanjing 210029, P. R. China

J. Shan
School of Pharmacy
The University of Sydney
Sydney, NSW 2006, Australia

The ORCID identification number(s) for the author(s) of this article can be found under https://doi.org/10.1002/adhm.202501008

DOI: 10.1002/adhm.202501008

and other illegal activities,[4] thus limiting its clinical application. Hence, the development of safe, abundant, and effective biomaterials is of great importance.

HAp is the primary inorganic component of human bone and closely resembles the mineral phase of bone tissue, making it a focus of research in bone repair biomaterials. Additionally, HAp exhibits excellent osteoconductive and osteoinductive properties.[5] Osteoconduction provides mechanical support for the growth of surrounding bone, while the osteoinductive property stimulates the differentiation of surrounding progenitor cells into osteoblasts. Thus, HAp scaffolds can provide spatial support for angiogenesis and new bone formation, while also inducing bone marrow stem cells (BMSCs) to differentiate into osteoblasts, accelerating bone regeneration and enhancing osteointegration.[6] Previous studies have shown that HAp materials play a key role in bone repair, particularly in promoting the differentiation of osteoblasts, bone mineralization, and new bone formation.[7] However, the biological functionality of pure HAp limitation remains. In contrast, natural bone tissue contains various trace elements that play important roles in metabolic processes during bone growth and repair.[8] Doping HAp with trace elements can endow it with enhanced biological functions, among which zinc (Zn) and magnesium (Mg) are essential trace elements closely related to bone metabolism.

Zn plays a crucial role in mineralization and osteoclast activity in the human body.[9] During bone formation, Zn promotes the proliferation and differentiation of osteoblasts and the synthesis of collagen.[10] It stimulates collagen synthesis, enhances alkaline phosphatase (ALP) activity, and induces the formation of bone nodules, thereby promoting mineralization at the site of bone defects. Additionally, Zn modulates the expression of Runt-related transcription factor 2 (RUNX2) to promote osteogenesis and regulates the Extracellular Signal-Regulated Kinase 1/2 (ERK1/2) signaling pathway in BMSCs to enhance bone formation.[11] Furthermore, Zn inhibits the Nuclear Factor Kappa-light-chain-enhancer of Activated B cells (NF-κB) activity in osteoclasts, stimulates their apoptosis, and reduces bone resorption. However, Zn exhibits a biphasic dose-response relationship in osteogenesis, with optimal effects observed at concentrations between 1–50 μM. Concentrations exceeding 50 μM can inhibit osteoblastic activity, while levels below 1 μM show no effect.[12] Liu et al. found that osteoblast activity gradually decreases with increasing Zn concentration. Moreover, they confirmed that Zn may regulate osteogenic and osteoclastic differentiation through the Wnt/β-catenin and NF-κB signaling pathways, respectively.[13]

Mg ions are also vital for bone mineralization and metabolism, affecting various cellular functions, including the transport of calcium (Ca) and potassium (K) ions, signal transduction, energy metabolism, and promoting cell proliferation.[14] Mg deficiency adversely impacts all stages of bone metabolism, leading to stunted growth, reduced osteoblastic activity, increased osteoclastic activity, decreased bone density, and increased fragility. Previous studies have shown that rats on a low-Mg diet exhibit reduced systemic bone density and suppressed growth of the proximal tibia, even presenting symptoms of osteoporosis.[15] Moreover, Mg ions induce angiogenesis in endothelial cells, primarily through increasing nitric oxide levels.[16] Mg also stimulates osteoblast adhesion and proliferation, induces osteogenic differentiation of mesenchymal stem cells, accelerates mineral deposition, reduces osteoclastic activity, and induces the secretion of anti-inflammatory cytokines.[17] Previous studies have suggested that the pro-osteogenic effect of Mg ions may be attributed to the synergistic activation of hypoxia-inducible factor (HIF)-2α and peroxisome proliferator-activated receptor gamma coactivator-1α (PGC-1α).[18] Thus, Zn/Mg co-doped HAp can enhance the biological functions of HAp and expedite the repair of bone defects.

However, pure HAp does not adhere well to the sites of bone defects, and the high-temperature sintering required for HAp scaffold preparation does not adequately match irregular bone defect shapes. Gelatin methacryloyl (GelMA), derived from the modification of gelatin with methacrylic anhydride, offers excellent biocompatibility, cell adhesion, and tunable mechanical properties.[19] Due to its similarity to the extracellular matrix, GelMA is particularly suitable for constructing bone tissue engineering scaffolds. By adjusting the concentration of GelMA, one can alter its porosity, stiffness, viscoelasticity, and degradation characteristics, which in turn affect cellular migration, survival, proliferation, and differentiation.[20] Compared to prefabricated solid materials, GelMA can be delivered via minimally invasive methods, reducing infection risks and enhancing comfort, while facilitating irregular bone defect areas. Furthermore, cells and bioactive molecules can be pre-mixed with the hydrogel material before injection, effectively overcoming challenges related to cell transplantation, adhesion, and delivery of bioactive molecules. Although the osteoinductive potential of Zn- and Mg-doped biomaterials has been widely reported, the spatial and temporal interplay between angiogenesis and osteogenesis in vivo remains underexplored. Here, we investigate Zn/Mg co-doped HAp-GelMA hydrogel scaffolds and their ability to simultaneously promote vascular and bone regeneration, supported by both histological and immunohistochemical evaluations.

As shown in **Figure 1**, in this study, we first synthesized Zn-doped HAp and Zn/Mg co-doped HAp using a hydrothermal method, then uniformly mixed the element-doped HAp with GelMA to prepare an injectable composite hydrogel for in vitro and in vivo studies on angiogenesis and bone regeneration repair. The resulting composite hydrogel exhibited good injectability and mechanical properties that meet the needs of bone tissue engineering. Additionally, the slow release of Zn reduced its cytotoxicity, while Mg promoted angiogenesis, thereby accelerating bone repair. Considering these advantages, we evaluated the potential of this injectable composite hydrogel as a biomaterial for the repair of bone defects. Additionally, we assessed its ability to promote bone repair in a rat cranial defect model.

2. Results and Discussion

2.1. Characterization of HA, Zn@HA, and Mg/Zn@HA

Using a hydrothermal synthesis method, HAp, Zn@HAp, and Mg/Zn@HAp powders were synthesized with the incorporation of Mg and Zn elements, utilizing H_6L as a small molecular template agent. The results of SEM (**Figure 2A**) indicated that the HAp powders in all groups exhibited a uniform spherical morphology with diameters ranging from 5 to 10 μm. The doping of Mg and Zn had a negligible effect on the morphology of

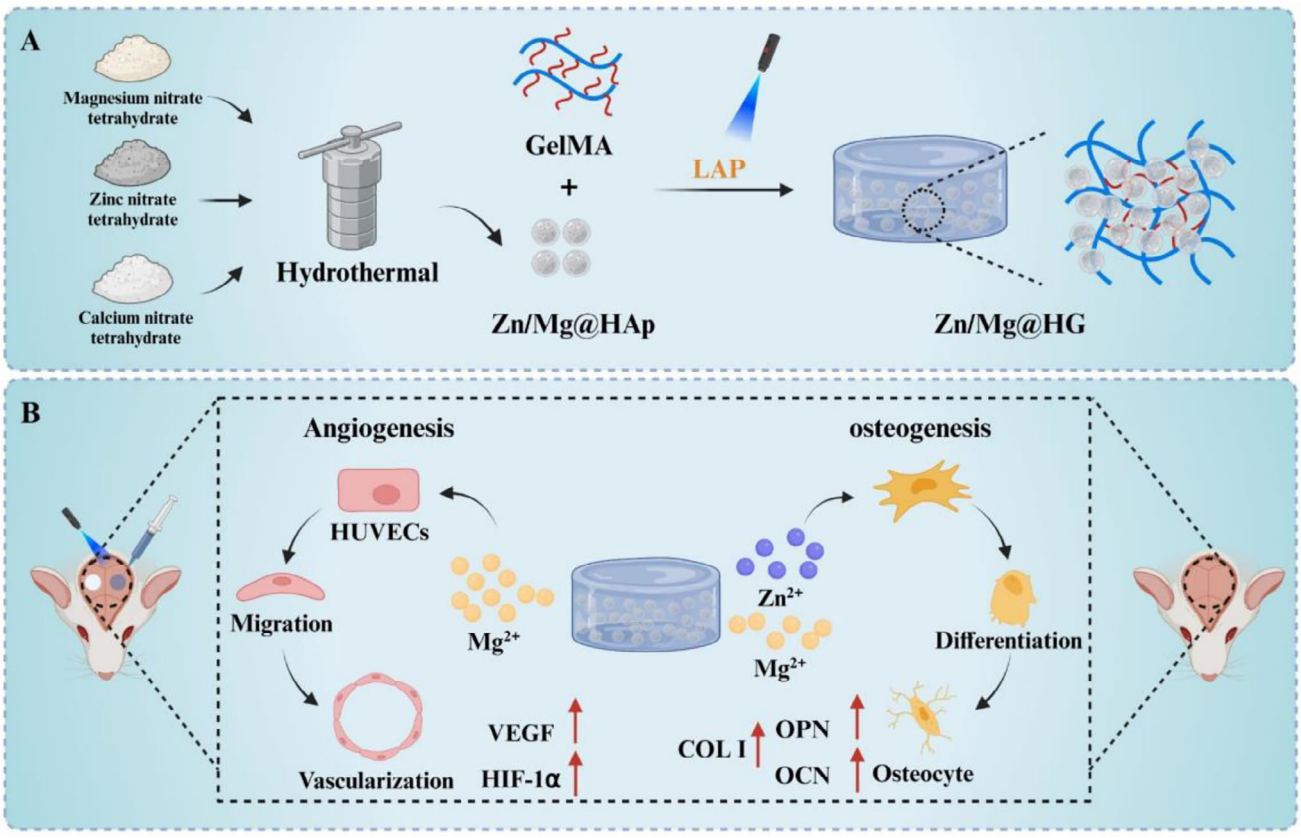

Figure 1. Schematic diagram of the preparation and function of Zn/Mg@HAp and Zn/Mg@HG for angiogenesis and osteogenesis (Created using BioRender.com).

the synthesized HAp. In addition, the particle size distribution showed that the particle size of each group was ≈5 μm (Figure S1, Supporting Information). The Previous study[21] showed that pure HAp synthesized without H_6L exhibited a needle-like crystal structure, while Zn-doped HAp displayed a more uniform microspherical morphology formed by stacked nanosheets. The addition of H_6L resulted in uniformly shaped microspheres for all HAp groups, which indicated its significant effect on morphology regulation.

The results of EDS (Figure 2A) demonstrated that Ca was uniformly distributed across all HAp powders. Zn was evenly distributed in the Zn@HAp and Mg/Zn@HAp powders, while Mg was only uniformly present on the surface of the Mg/Zn@HAp powders. ICP analysis ($n = 4$) showed Zn@HA contained 4.880 ± 0.021 wt.% Zn, while Mg/Zn@HA had 0.821 ± 0.015 wt.% Mg and 4.724 ± 0.019 wt.% Zn.

XRD was performed to validate the phase composition of the synthesized HAp, focusing on the crystalline structure and the effects of Mg and Zn on the crystallinity and lattice parameters, such as crystal growth direction. The results (Figure 2B) indicated that all three samples contained characteristic peaks of HAp without any additional phase peaks. Compared to the standard card for HAp (JCPDS09-0432),[22] the intensity ratio $I_{(300)}/I_{(211)}$ of pure HAp (65%) was higher than the standard HAp (60%), while the $I_{(002)}/I_{(300)}$ ratio (69%) also exceeded that of the standard HAp (66.7%). This demonstrates that the HAp crystals grew along both the a-axis and c-axis during synthesis, tending toward a spherical structure, consistent with the SEM results. These results differ from the results of HAp synthesized without H_6L[21] suggesting that the addition of H_6L promotes isotropic growth of HAp crystals. After doping with Zn ions, the $I_{(300)}/I_{(211)}$ ratio increased to 77%, while the $I_{(002)}/I_{(300)}$ ratio (65%) was close to that of the standard HAp, indicating an increase in growth along the a-axis with unchanged c-axis growth, favoring irregular spherical structures. The incorporation of Mg ions led to significant increases in both the $I_{(300)}/I_{(211)}$ (82%) and $I_{(002)}/I_{(300)}$ ratios (72%), further promoting the spherical structure, thus confirming that both H_6L and trace elements can modulate the morphology of HAp.

FT-IR was used To further verify the chemical structure of the synthesized Hap by identifying the functional groups present in the samples. The FT-IR spectra (Figure 2C) revealed characteristic peaks for HAp in all groups. The bending and stretching vibration peaks of P—O in PO_4^{3-} were located at 560 and 600 cm^{-1}, and at 959, 1020, and 1088 cm^{-1}, respectively. A characteristic peak at 3340 cm^{-1} represented the stretching vibration of H—O in free H_2O molecules adsorbed on the material's surface, while the bending vibration peak of H-O mainly appeared at 1600 cm^{-1}. Additionally, C-O characteristic peaks at 874 and 1400 cm^{-1} indicated a minor A-type and B-type substitution of

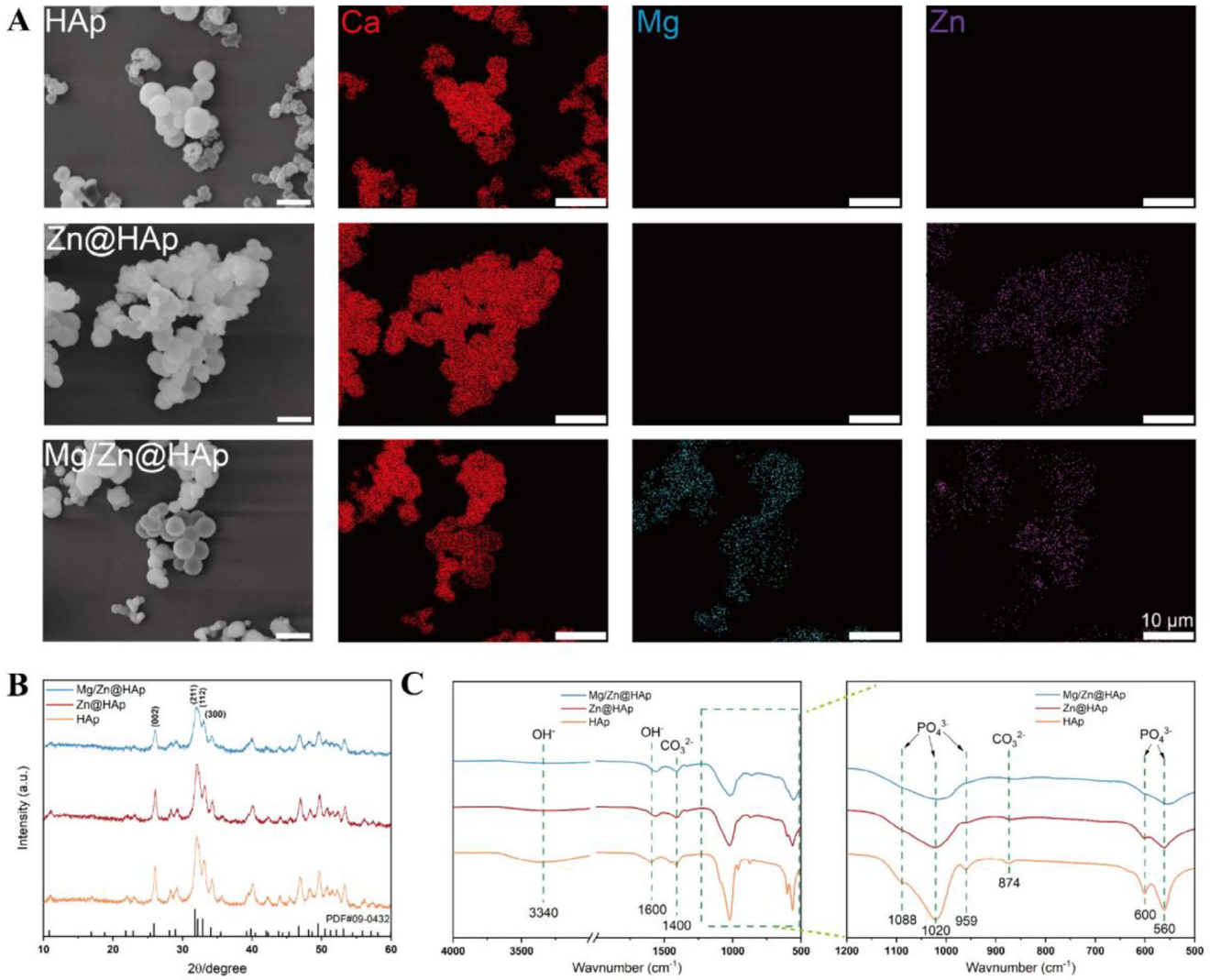

Figure 2. Characterization of HAp, Zn@HAp, and Zn/Mg@HAp. A) SEM images and element mapping, B) XRD patterns, and C) FT-IR spectra. Scale = 10 μm.

CO_3^{2-} at the PO_4^{3-} and OH^- positions.[23] The presence of the absorption peak for CO_3^{2-} may result from CO_2 in the air dissolving into the liquid during the synthesis process, leading to the incorporation of some CO_3^{2-} into the HAp lattice, substituting for PO_4^{3-}. Notably, human bone mineral composition contains a small amount of carbonate apatite, and HAp with carbonate substitution shows improved biocompatibility compared to pure HAp.[24]

2.2. Characterization of Injectability and Photocrosslinking of Element-Doped HAp-GelMA Composite Hydrogel

To fabricate composite hydrogel scaffolds, the synthesized element-doped HAp powders were mixed with GelMA to form prepolymer solutions, labeled as 0.5%HG, 0.5%Zn@HG, 0.5%Mg/Zn@HG, 1%HG, 1%Zn@HG, 1%Mg/Zn@HG, 2%HG, 2%Zn@HG, and 2%Mg/Zn@HG. The injectability and photocrosslinking properties were first evaluated. Using the 2%Mg/Zn@HG as an example, the results (Figure S2, Supporting Information) indicated that the uncrosslinked prepolymer solution could be easily extruded from the syringe at room temperature, demonstrating good injectability.

Subsequently, the prepolymer solution was transferred to a round-bottom glass bottle, which was tilted (**Figure 3B**). After 10 s of exposure to 405 nm blue-violet light, the flow behavior of the hydrogel was observed to preliminarily assess the photocrosslinking performance. Before illumination, the 2%Mg/Zn@HG prepolymer solution appeared as a milky, flowing liquid, which transformed into a milky, opaque gel after 10 s of light exposure. The sample exhibited excellent viscosity and filling capability, rapidly crosslinking at the site of application upon blue-violet light exposure, providing a feasible approach for filling and treating bone defects in clinical applications.

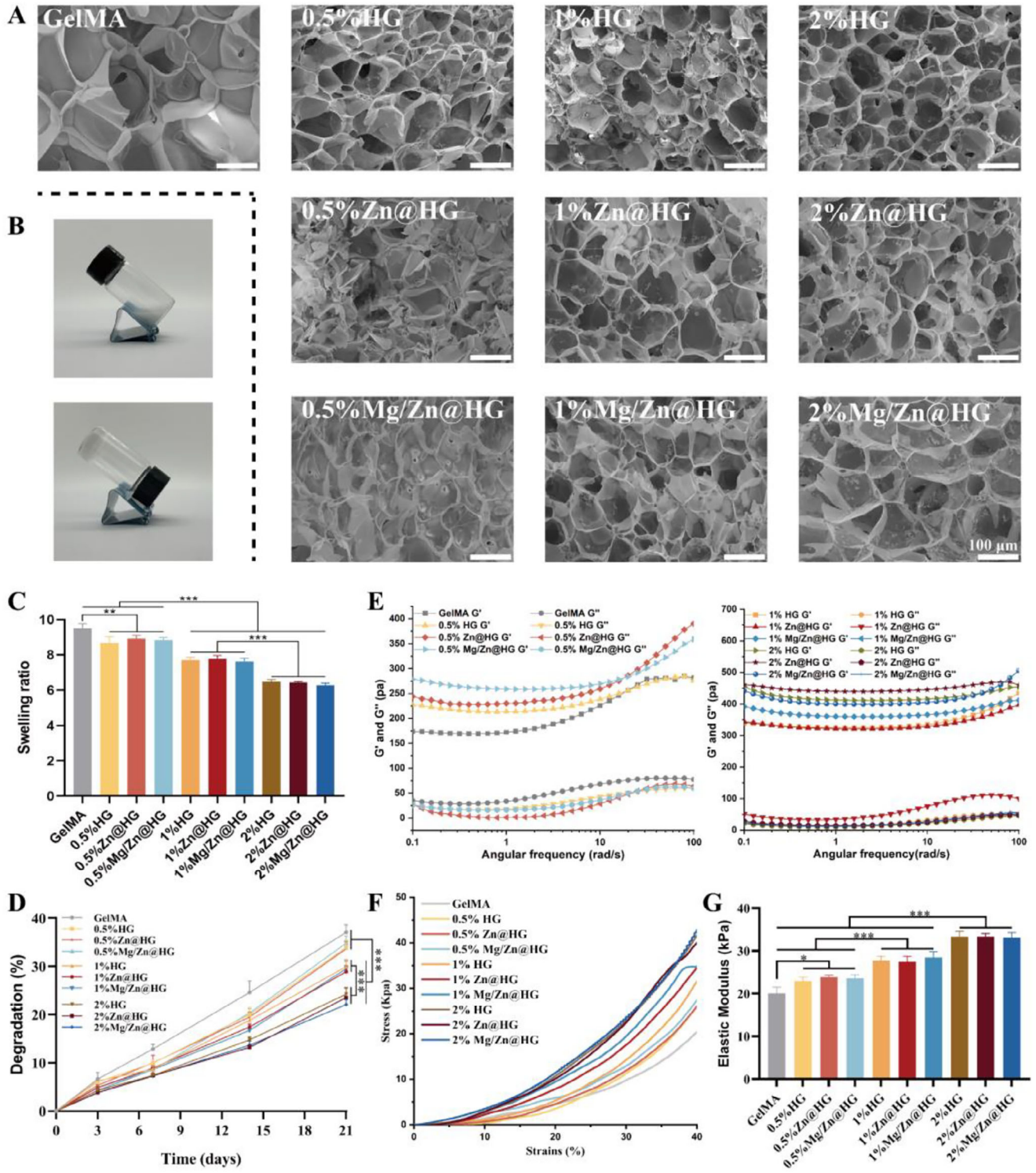

Figure 3. Characterization of composite hydrogel. A) SEM images, B) Gelation diagram, C) Swelling ratio, D) Degradation ratio, E) Rheological properties, F) Stress–strain curve, and G) Elastic modulus. Scale = 100 μm. ($^{*}p < 0.05$, $^{**}p < 0.01$, $^{***}p < 0.001$, $n = 4$).

2.3. Morphology, Porosity, Element Distribution, and Phase Composition of Element-Doped HAp-GelMA Composite Hydrogels

Figure S3 (Supporting Information) shows the optical images of the composite hydrogel scaffolds for each group. Upon observing the morphology of the composite hydrogels after curing, it could be seen that as the content of HAp, Zn@HAp, and Mg/Zn@HAp increased, the color of the composite hydrogels changed from transparent to white and gradually darkened.

The composite hydrogels were subjected to cryogenic fracturing using liquid nitrogen, and their fracture morphology was observed via SEM. EDS was also employed for elemental detection and distribution analysis of the composite hydrogels. The SEM results (Figure 3A) indicated that all groups exhibited a sponge-like, porous network structure. As the concentration of HAp increased, the overall pore size of the composite hydrogels tended to decrease, while the interconnected porous network was preserved. HAp was uniformly distributed on the pore walls, which became thicker and rougher, with trace elements being evenly distributed on the surface. Further analysis of the pore size of the composite hydrogels in each group revealed (Figure S4A, Supporting Information) that the average pore size of the GelMA group was 176.44 ± 33.76 μm. As the content of HAp increased, the average pore size of the composite hydrogels gradually decreased to 43.12 ± 9.04 μm in the 2% Zn@HG group. However, the porosity of the hydrogels in each group (Figure S4B, Supporting Information) did not show significant differences due to the addition of HAp.

For elemental distribution analysis, the 2% HAp-doped group was selected. The EDS results (Figure S5, Supporting Information) demonstrated that Ca was uniformly distributed across all composite hydrogels, while Zn was evenly distributed in the Zn@HG and Mg/Zn@HG groups, and Mg was only found on the surface of the Mg/Zn@HG group. The microstructure of GelMA is highly suitable for the incorporation of magnesium and zinc ion-doped ceramic powders, while the interconnected pores facilitate the migration and adhesion of cells at high densities.[25]

To verify the phase composition within the composite hydrogels, we characterized their FTIR spectra. The results (Figure S6, Supporting Information) demonstrated that all groups exhibit characteristic peaks of GelMA. Notably, the groups containing HA and element-doped HA variants show characteristic peaks of PO_4^{3-} at 959, 1020, and 1088 cm^{-1} (highlighted in light yellow), which indicates that GelMA and HA (along with its doped variants) collectively constitute the chemical phase components of the composite hydrogels.

2.4. Element-Doped HAp Reduces the Swelling Ratio and Degradation Rate of Composite Hydrogels

Due to the hydrophilic nature of hydrogels, they tend to absorb and retain moisture within their polymer networks. Hydrogels with good swelling performance facilitate the exchange of nutrients and metabolic waste for cells. As shown in Figure 3C, after 24 h of swelling in PBS, GelMA hydrogels reached a swelling ratio of 9.5 ± 0.27 times their dry weight. As the proportion of HAp in the material increased, the swelling ability of the composite hydrogels gradually decreased: the swelling ratio for 0.5%HG was 8.68 ± 0.34 times, for 1%HG was 7.7 ± 0.15 times, and 6.48 ± 0.12 times for 2%HG. This reduction reflects the stability of the material; the addition of HAp enhances the stability of GelMA, and with increasing doping concentration, the crosslinking density also increases, leading to a lower water absorption swelling rate.

Furthermore, the degradation rates of the hydrogels in vitro were observed (Figure 3D). As the proportion of HAp increased, the degradation time of the composite hydrogels was prolonged. GelMA lost ≈37.04 ± 1.54% of its dry weight by day 21, while 0.5%HG lost 33.93 ± 1.45%, 1%HG lost 29.9 ± 1.53%, and 2%HG lost only 24.2 ± 1.42%. This correlates with the swelling results, indicating that HAp increases the crosslinking density of GelMA, thereby enhancing its stability and making the 3D crosslinked network less prone to degradation. Previous studies have shown[26] that the dissolution of chemical bonds accelerates the erosion of composite hydrogels, leading to a more loosened network structure. Additionally, due to the higher content of HAp in composite hydrogels with a higher concentration of HAp, these hydrogels exhibit a higher mass residue percentage after the degradation of the gel components. Therefore, the degradation rate can be adjusted by modifying the ratio of GelMA to HAp microspheres in the composite hydrogel to meet the requirements of bone tissue engineering.

2.5. Element-Doped HAp Significantly Improves the Mechanical Properties of Composite Hydrogels

The rheological properties of the composite hydrogels are shown in Figure 3E. All groups exhibited relatively stable storage modulus (G') and loss modulus (G""), and regardless of frequency, the curves for G' and G"" did not converge, with G' significantly greater than G"". This indicates that all composite hydrogels were successfully crosslinked and remained stable in a gel state. With the increasing amount of HAp powder, the G' values of the composite hydrogels also increased, indicating that higher concentrations of HAp enhanced the hardness of GelMA.

Moreover, the stress–strain testing results (Figure 3F) showed that as the proportion of HAp increased, the compressive strength improved, leading to better mechanical performance of the hydrogels. The elastic modulus of GelMA was 20.06 ± 1.46 kPa, which gradually increased to 33.3 ± 1.29 kPa as the content of HAp in the composite hydrogels increased (Figure 3G). Research indicates that stem cells can sense the mechanical properties of their environment, suggesting that the mechanical properties of the extracellular matrix can regulate stem cell differentiation.[27] Environments with an elastic modulus of 2.5–5 kPa promote adipogenic differentiation, while those with an elastic modulus of 15–30 kPa favor osteogenic differentiation.[28] The mechanical properties of the synthesized composite scaffolds align with the requirements for osteogenesis. Previous studies have shown[26,29] that HAp can improve the mechanical properties of GelMA. When combined with GelMA, it significantly enhances the mechanical performance of GelMA, and this improvement increases with the concentration of HAp. However, excessive HAp may reverse this trend, which could be due to the increased concentration of HAp decreasing

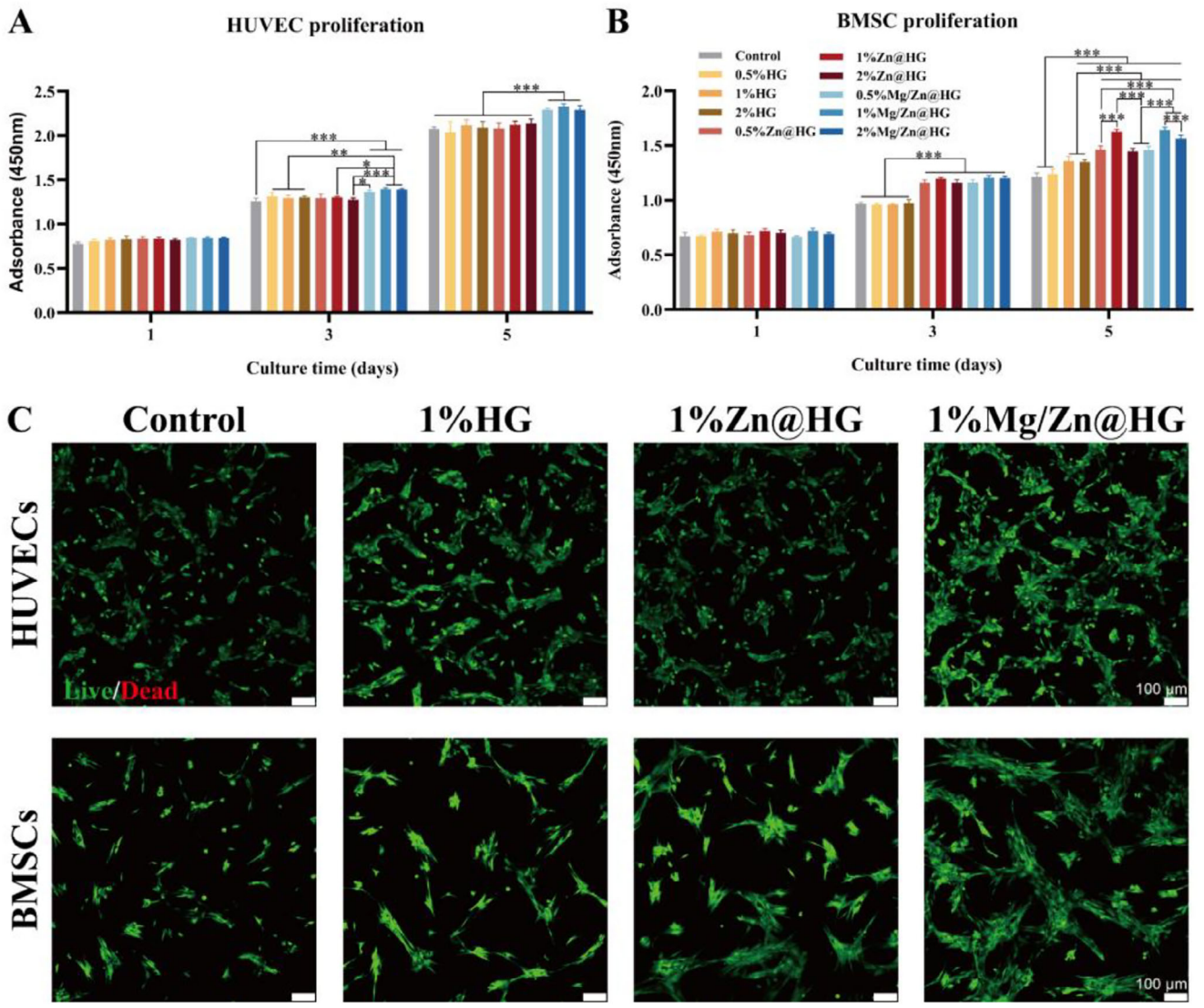

Figure 4. Proliferation activity of composite hydrogels after co-culture with A) HUVEC and B) rBMSCs for 1, 3, and 5 days, and C) Cytotoxicity of 1% HG, 1% Zn@HG, and 1% Mg/Zn@HG after co-culture with HUVECs and BMSCs for 3 days. Scale bar = 100 μm. ($^{*}p < 0.05$, $^{**}p < 0.01$, $^{***}p < 0.001$, $n = 4$).

the hydrogel's transparency, thus reducing the intensity of UV crosslinking. On the other hand, because HAp is crystalline in nature, it absorbs and interferes with ultraviolet light, which decreases the effect of UV crosslinking. The degree of crosslinking, in turn, affects the pore size and mechanical strength of the HAp/GelMA hydrogel.[26]

Finally, the cumulative release of Zn and Mg from the composite scaffolds was evaluated in simulated in vitro environments (Figure S7, Supporting Information). All groups exhibited stable and sustained release effects over 14 days. The release rate of Zn ions increased with the addition of Mg ions, and the concentrations of released Zn and Mg also rose with the increasing concentration of element-doped HAp.

2.6. Effects of Composite Hydrogel Scaffolds on Proliferation and Viability of rBMSCs and HUVEC

This study investigated the cytotoxicity of composite hydrogel scaffolds and their effects on cell proliferation. The CCK-8 assay was conducted to evaluate the impact of the scaffolds on the proliferation of rBMSCs and HUVECs. The results (**Figure** 4A,B) showed no statistically significant differences in rBMSCs viability among the groups on day 1. However, by day 3, the rBMSCs viability in the experimental groups containing Zn^{2+} showed an increase. By day 5, the RBMSC viability in the 1%Zn@HG and 1%Mg/Zn@HG groups was higher than in the other groups, indicating a favorable effect on promoting RBMSC proliferation.

Similarly, on day 1, there were no significant differences in HUVEC viability among the groups. On days 3 and 5, the composite hydrogel scaffolds containing Mg^{2+} enhanced HUVEC proliferation. These results suggest that all experimental groups exhibited good biocompatibility for both rBMSCs and HUVECs, with the 1%Mg/Zn@HG scaffold demonstrating the best proliferative effects for both cell types. Therefore, the 1%HG, 1%Zn@HG, and 1%Mg/Zn@HG groups were selected for subsequent experiments.

Next, live/dead staining was performed to assess the cytotoxicity of the three composite hydrogel scaffolds (1%HG, 1%Zn@HG, and 1%Mg/Zn@HG). The results (Figure 4C) indicated that rBMSCs and HUVECs on the surfaces of all hydrogel groups maintained normal shapes, with viable cells predominating and only a few dead cells present. This demonstrated good cell vitality and indicated that all hydrogel groups possessed excellent biocompatibility. Notably, the 1%Mg/Zn@HG group exhibited the largest cell spreading area among all experimental groups, aligning with the CCK-8 results.

2.7. Evaluation of In Vitro Angiogenic Ability of Composite Hydrogel Scaffolds

To further evaluate the angiogenic capability of the Mg-containing composite hydrogel scaffolds, tube formation assays were performed. The results (**Figure 5**A) demonstrated that both the 1%Zn@HG and 1%Mg/Zn@HG groups exhibited significantly enhanced tubular network formation compared to the Control and 1%HG groups. Statistical analysis revealed that the 1%Mg/Zn@HG group formed a greater number of capillary-like structures, outperforming the other groups in tube count (Figure 5C).

Subsequently, wound healing assays were conducted to assess the ability of the composite hydrogels to promote HUVEC migration. The results (Figure 5B) showed cell migration across all groups, with no significant differences in migration observed among groups lacking Mg^{2+}. However, the 1%Mg/Zn@HG group had markedly increased cell migration at both 24 and 48 h. Quantitative analysis (Figure 5D) further confirmed that the 1%Mg/Zn@HG group wound healing rates were superior at both time points, reaching up to 72% closure at 48 h, indicating that Mg ions significantly enhance HUVEC migration.

Bone injury sites are characterized by Hypoxic conditions and elevated lactate levels, inducing stable expression of HIF-1α.[30] HIF-1α drives VEGF expression, thereby promoting angiogenesis.[30b] Some previous studies have shown that Mg can upregulate VEGF expression, indicating its angiogenic potential.[31] Thus, we assessed the expression of angiogenesis-related genes and proteins via RT-qPCR and Western blotting. Both HIF-1α and VEGF were expressed at higher levels in all experimental groups compared to the Control, with the Mg^{2+}-containing group showing the highest expression levels (Figure 5E). VEGF stimulates endothelial cell proliferation and sprouting, while its inhibition or lack can diminish angiogenic potential and reduce the quality of newly formed tissue at the injury site.[32] Additionally, Western blot results (Figure 5F; Figure S8 Supporting Information) confirmed that the 1%Mg/Zn@HG group had higher expressions of HIF-1α and VEGF than the other groups, consistent with gene expression findings. These results indicate that the 1%Mg/Zn@HG group possesses superior angiogenic capabilities compared to the other groups.

2.8. Evaluation of In Vitro Osteogenic Performance of Composite Hydrogel Scaffolds

To assess the osteogenic capabilities of the composite hydrogel scaffolds, ALP staining was performed on days 7 and 14 of osteogenic induction. The results (**Figure 6**A) revealed blue-purple deposits, indicative of the presence of ALP, with the 1%HG, 1%Zn@HG, and 1%Mg/Zn@HG groups exhibiting deeper coloration compared to the control group. Notably, on day 14, the 1%Mg/Zn@HG group displayed the most intense color and a larger stained area than the other groups. Quantitative analysis (Figure 6B) confirmed these findings, indicating that the 1%Mg/Zn@HG group had the highest alkaline phosphatase activity, indicating enhanced early osteogenesis.

After 21 days of osteogenic induction, ARS staining results (Figure 6A) demonstrated that the 1%HG, 1%Zn@HG, and 1%Mg/Zn@HG groups formed significantly more mineralized nodules compared to the control group, with the 1%Mg/Zn@HG group yielding the highest number. Semi-quantitative analysis of ARS (Figure 6C) further confirmed that the 1%Mg/Zn@HG group had the greatest capacity for calcium salt deposition and calcified nodule formation during the later stages of osteogenesis.

To further evaluate the influence of the composite hydrogel scaffolds on bone formation, rBMSCs were co-cultured with the scaffold extracts for 14 days, after which key osteogenic target genes and proteins were measured. Osteocalcin (OCN), osteopontin (OPN), and collagen I (COL I) are all markers of osteoblast activity. The results (Figure 6D) showed that the expression of these osteogenic-related genes significantly increased in the 1%HG, 1%Zn@HG, and 1%Mg/Zn@HG groups, with the 1%Mg/Zn@HG group exhibiting the highest osteogenic activity.

Western blot analysis (Figure 6E; Figure S9 Supporting Information) revealed that the protein expression levels of OPN and COL I were higher in the 1%Zn@HG and 1%Mg/Zn@HG groups compared to the control and 1%HG groups, with the 1%Mg/Zn@HG group showing elevated OPN levels compared to the 1%Zn@HG group, consistent with gene expression data. This indicates that Mg and Zn ions can synergistically promote bone formation, which may be closely related to Mg's role in enhancing angiogenesis—an essential process in bone development. Magnesium-induced angiogenic factors (e.g., VEGF from endothelial cells) enhance the osteogenic differentiation of nearby stem cells, which is reflected in the upregulation of bone matrix proteins like OPN. In our co-culture/conditioned medium environment, the presence of Mg^{2+} likely elevated angiogenic signaling, thereby secondarily boosting OPN expression in osteogenic cells. Blood vessels not only supply nutrients to bone tissue but also promote the proliferation and differentiation of bone cells, thereby supporting bone regeneration and repair. The 1%Mg/Zn@HG composite hydrogel scaffolds facilitate the co-promotion of angiogenesis and osteogenesis, effectively reconstructing a vascularized bone microenvironment.

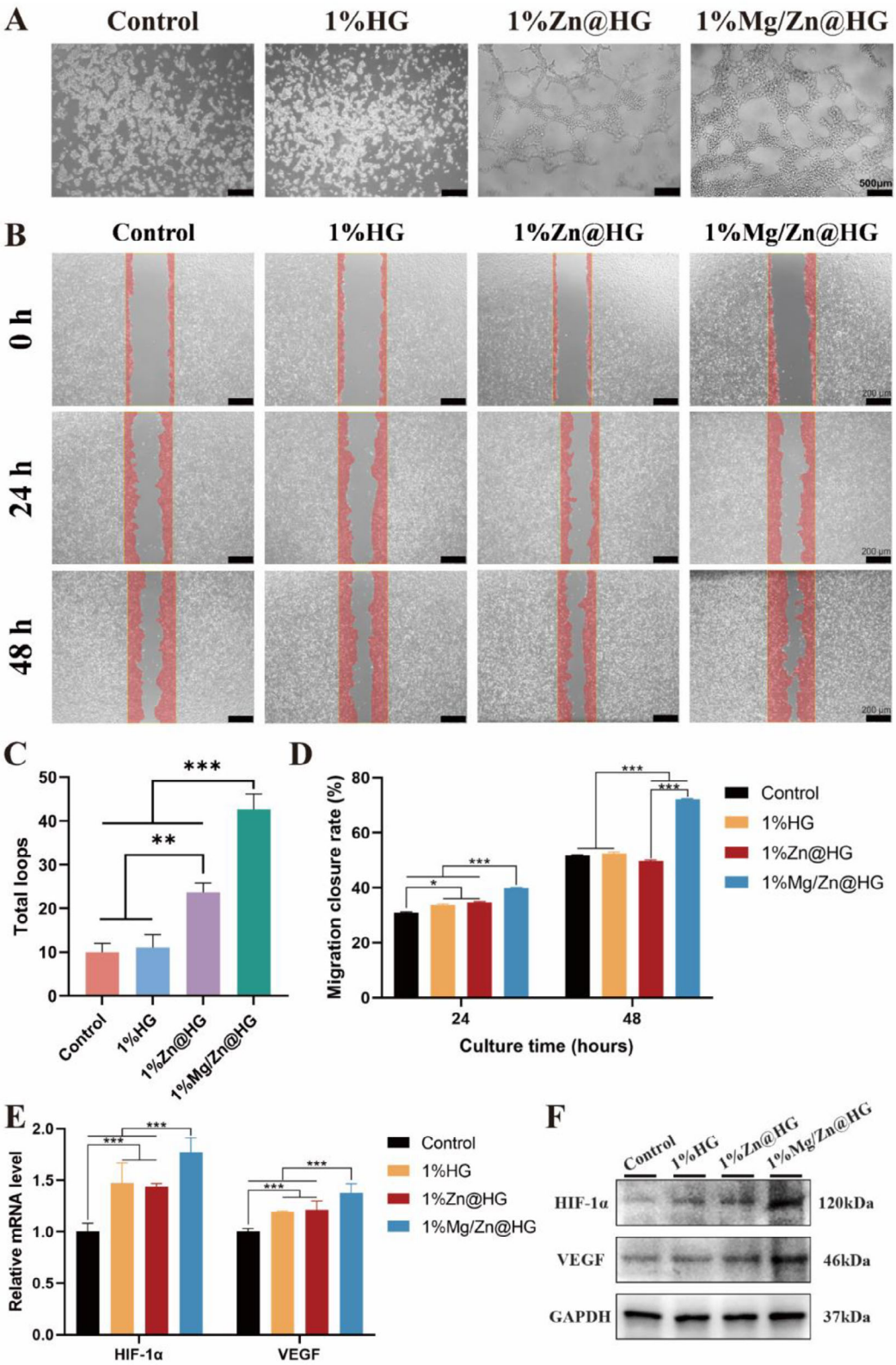

Figure 5. Characterization of angiogenesis of composite hydrogels. A) Angiogenesis of Matrigel, B) Cell migration, C) Statistical results of the number of angiogenesis, D) Statistical results of cell migration rate, E) Angiogenesis-related gene expression of composite hydrogel scaffolds, and F) Angiogenesis-related protein expression of composite hydrogel scaffolds. Scale = 200 μm. ($^{*}p < 0.05$, $^{**}p < 0.01$, $^{***}p < 0.001$, $n = 4$).

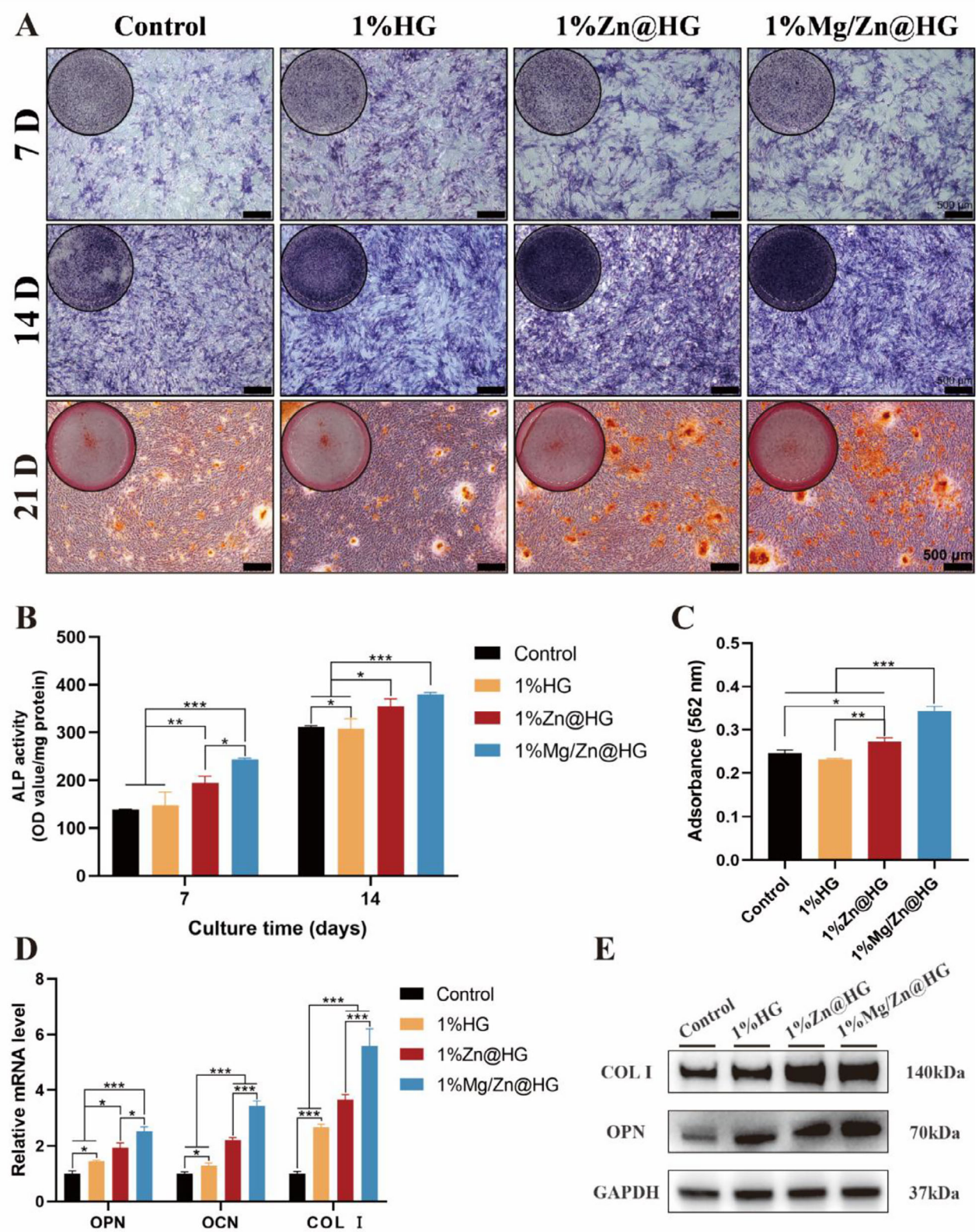

Figure 6. In vitro evaluation of the osteogenic capacity of the composite hydrogel scaffolds. A) ALP staining of cells cultured for 7 and 14 days and ARS staining of cells on day 21, B) ALP activity of cells cultured for 7 days, C) Quantification of cell mineralization on day 21, D) Osteogenesis-related gene expression of composite hydrogel scaffolds, and E) Osteogenesis-related protein expression of composite hydrogel scaffolds. Scale = 500 μm. ($^{*}p < 0.05$, $^{**}p < 0.01$, $^{***}p < 0.001$, $n = 4$).

In summary, in vitro experiments demonstrate that the 1%Mg/Zn@HG composite hydrogel effectively promotes angiogenic factor secretion, inducing the osteogenic differentiation of BMSCs, thereby achieving bone defect repair.

2.9. In Vivo Evaluation of Osteogenesis Induced by Composite Hydrogel Scaffolds

To further evaluate the bone regeneration capability of the injectable Zn/Mg@HG composite hydrogel in vivo, a rat cranial defect model was established, and three groups of composite hydrogels were injected in situ. Micro-CT and histological analyses were conducted to assess the effects of the composite hydrogels on cranial bone regeneration at 6 and 12 weeks post-implantation.

Micro-CT results (**Figure** 7A; Figure S10 Supporting Information) revealed that at 6 weeks, both the 1%Zn@HG and 1%Mg/Zn@HG groups demonstrated significantly enhanced bone formation compared to the control and 1%HG groups, with the 1%Mg/Zn@HG group exhibiting the greatest amount of new bone formation. This group had the largest area of new bone and the smallest residual defect area, whereas the control group showed minimal new bone ingrowth. By 12 weeks, the defect site in the 1%Mg/Zn@HG group was almost filled with new bone tissue, consistent with the trend observed at 6 weeks. Quantitative analysis of Micro-CT data (Figure 7B–E) provided insights into related bone tissue parameters. The ratio of bone tissue volume to total volume (BV/TV) indicated changes in bone quantity, showing significantly higher BV/TV values for the 1%Zn@HG and 1%Mg/Zn@HG groups, with the latter achieving the highest BV/TV. Bone mineral density (BMD), reflecting bone tissue density, followed a similar trend. Furthermore, trabecular thickness (Tb.Th) and trabecular separation (Tb.Sp) were utilized to evaluate the microstructure and maturity of the bone tissue. The 1%Mg/Zn@HG group displayed higher Tb.Th and lower Tb.Sp compared to the control, 1%HG, and 1%Zn@HG groups, indicating a more mature development of new bone tissue in this group. These results demonstrate that the 1%Mg/Zn@HG group achieved superior new bone integration, successfully repairing critical-sized bone defects.

Histological examination using H&E and Masson staining further elucidated the impact of the composite hydrogel scaffolds on bone regeneration. As shown in **Figures** 8 and S11 (Supporting Information), no significant signs of inflammation or necrosis were observed in the histological sections of all experimental groups post-implantation, indicating the excellent biocompatibility of the composite hydrogel scaffolds. At the 6-week time point, no new bone formation was evident in the control and 1%HG groups, whereas both the 1%Zn@HG and 1%Mg/Zn@HG groups filled the defects and exhibited new bone formation, with the 1%Mg/Zn@HG group showing a greater area of new bone. As implantation time increased to 12 weeks, all groups (1%HG, 1%Zn@HG, and 1%Mg/Zn@HG) demonstrated new bone formation, with increased new bone quantity compared to the 6-week time point. Notably, the 1%Mg/Zn@HG group exhibited the highest amount of new bone tissue and the largest new bone area, while the control group only displayed sparse fibrous tissue in the defect region. Masson staining corroborated these findings, revealing greater collagen deposition in the 1%Mg/Zn@HG group.

To investigate vascularization associated with the implanted hydrogels, immunohistochemical staining for VEGF, CD31, and α-SMA was conducted on bone defect sections harvested at 6 and 12 weeks post-operation. Representative staining images are presented in **Figure** 9. VEGF staining was visibly more pronounced in the 1%Zn@HG group at 12 weeks, suggesting an enhanced pro-angiogenic response in the presence of zinc doping. CD31 and α-SMA staining were detectable across all groups, with relatively more distinct vessel-like structures observed in the co-doped groups. These findings are consistent with the known roles of Zn^{2+} and Mg^{2+} ions in promoting endothelial activation and vascular maturation, respectively.

The results indicate that the angiogenic potential of Mg ions facilitates vascularization at the defect site, enhancing the exchange of cellular waste and nutrients for newly formed bone. Additionally, both Mg and Zn promote osteogenesis, with the incorporation of Mg ions synergistically enhancing the bone formation facilitated by Zn ions.

The composite hydrogels synthesized in this study exhibit a porous structure with the ability to promote osteogenic differentiation of rBMSCs, showing great potential in bone healing. This porous structure can improve nutrient transport and waste removal, providing a strong microenvironment for the proliferation and differentiation of rBMSCs.[33] Additionally, Mg ions have the potential to promote angiogenesis by enhancing the expression of angiogenesis-related proteins (VEGF, HIF-1α), thus facilitating tube formation and vascularization.[34] Osteogenesis and angiogenesis are closely related, mutually dependent, and supportive. Osteoblasts can promote vascular formation and influence its activity by secreting angiogenesis-related substances, while endothelial cells produce vascular-secreted signals to regulate bone remodeling and repair.[35] At the same time, Mg ions can also inhibit the activity of osteoclasts[36] and reduce the ratio of M1/M2 macrophages, promoting the osteogenic potential of BMSCs.[37] On the other hand, relevant studies have shown that Zn ions possess both osteogenic and antibacterial activities.[38] However, excessive concentrations of Zn may induce toxicity in vivo, posing a potential safety concern.[39] High doses and concentrations of Zn ions are harmful because their intracellular accumulation can lead to mitochondrial damage and disruption of Zn homeostasis.[40] Therefore, controlled release of Zn ions can not only reduce cytotoxicity but also harness their potential to promote osteogenic differentiation of stem cells. Moreover, Mg ions have been reported to promote angiogenesis[41] and bone repair.[42] Zheng et al.[43] found that Mg ions can stimulate the secretion of calcitonin gene-related peptide-α (CGRP) by neurons in the cortex around the femur and in the ipsilateral dorsal root ganglia, thereby promoting fracture healing. Another study[42b] revealed that Mg can accelerate the repair of critical-sized bone defects during distraction osteogenesis. The underlying mechanism may involve the activation of the CGRP-FAK-VEGF signaling axis in sensory neurons and endothelial cells. Specifically, Mg stimulates sensory neurons to secrete CGRP, and the increased CGRP further enhances angiogenesis by activating the FAK-VEGF signaling pathway in endothelial cells. Consequently,

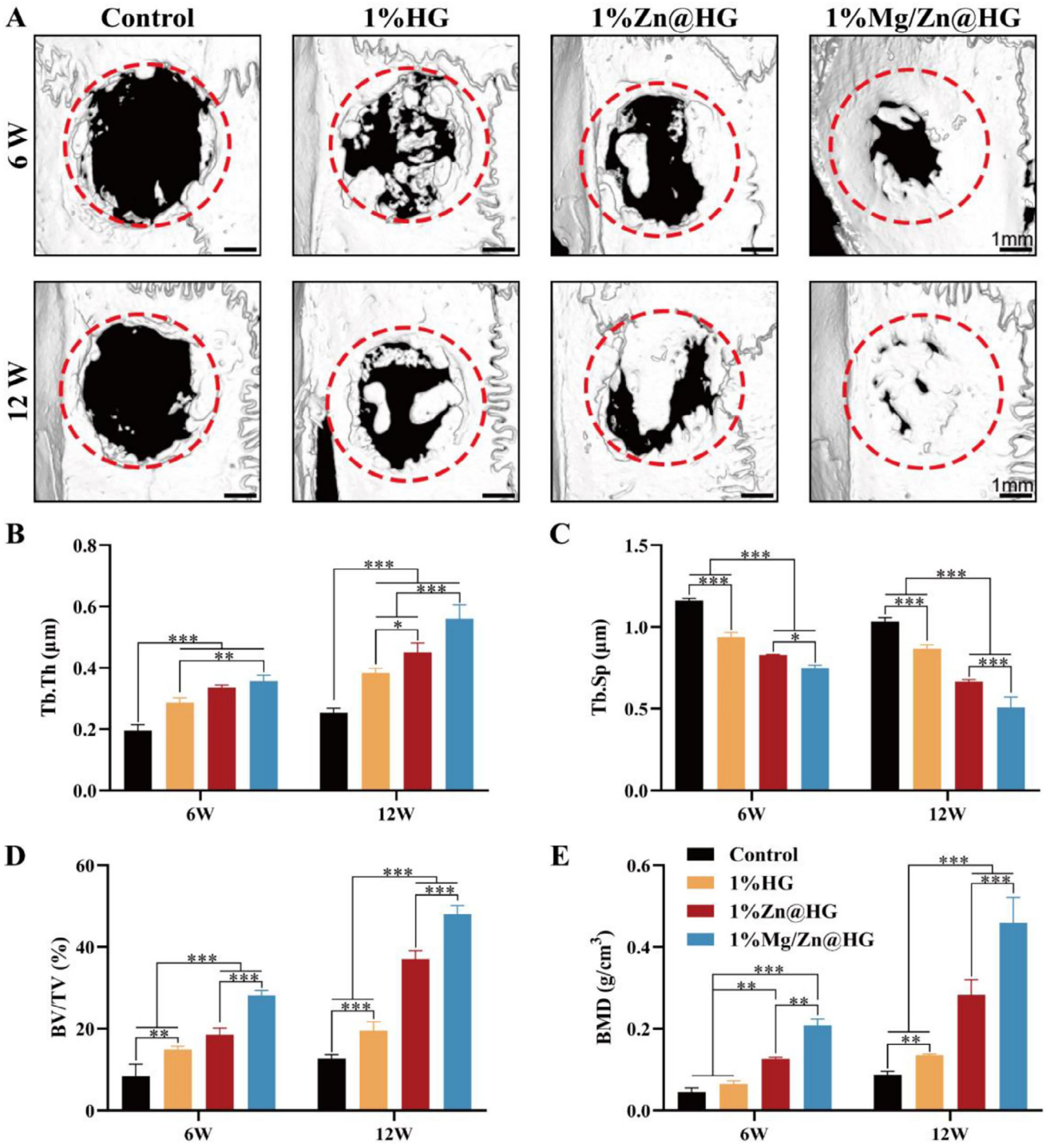

Figure 7. Micro-CT analysis of bone regeneration in composite hydrogel scaffolds. A) 3D Micro-CT reconstruction images of in vivo bone defect repair at 6 and 12 weeks (scale bar = 1 mm), B) Tb·Th, C) Tb·Sp, D) BV/TV, and E) BMD analysis. ($^{*}p < 0.05$, $^{**}p < 0.01$, $^{***}p < 0.001$, $n = 4$).

co-doping hydroxyapatite (HA) with Zn and Mg can not only enable the slow and safe release of Zn ions but also synergistically enhance angiogenesis to facilitate bone regeneration. In this chapter, the bone formation and ossification in the Mg/Zn co-doped hydrogel group were significantly greater than in the groups without Mg/Zn or with only Zn, indicating that Zn and Mg ions can synergistically promote osteogenic differentiation and accelerate bone repair. The injectability and bone repair potential of this composite hydrogel lay a solid foundation for its application in bone repair and regenerative medicine.

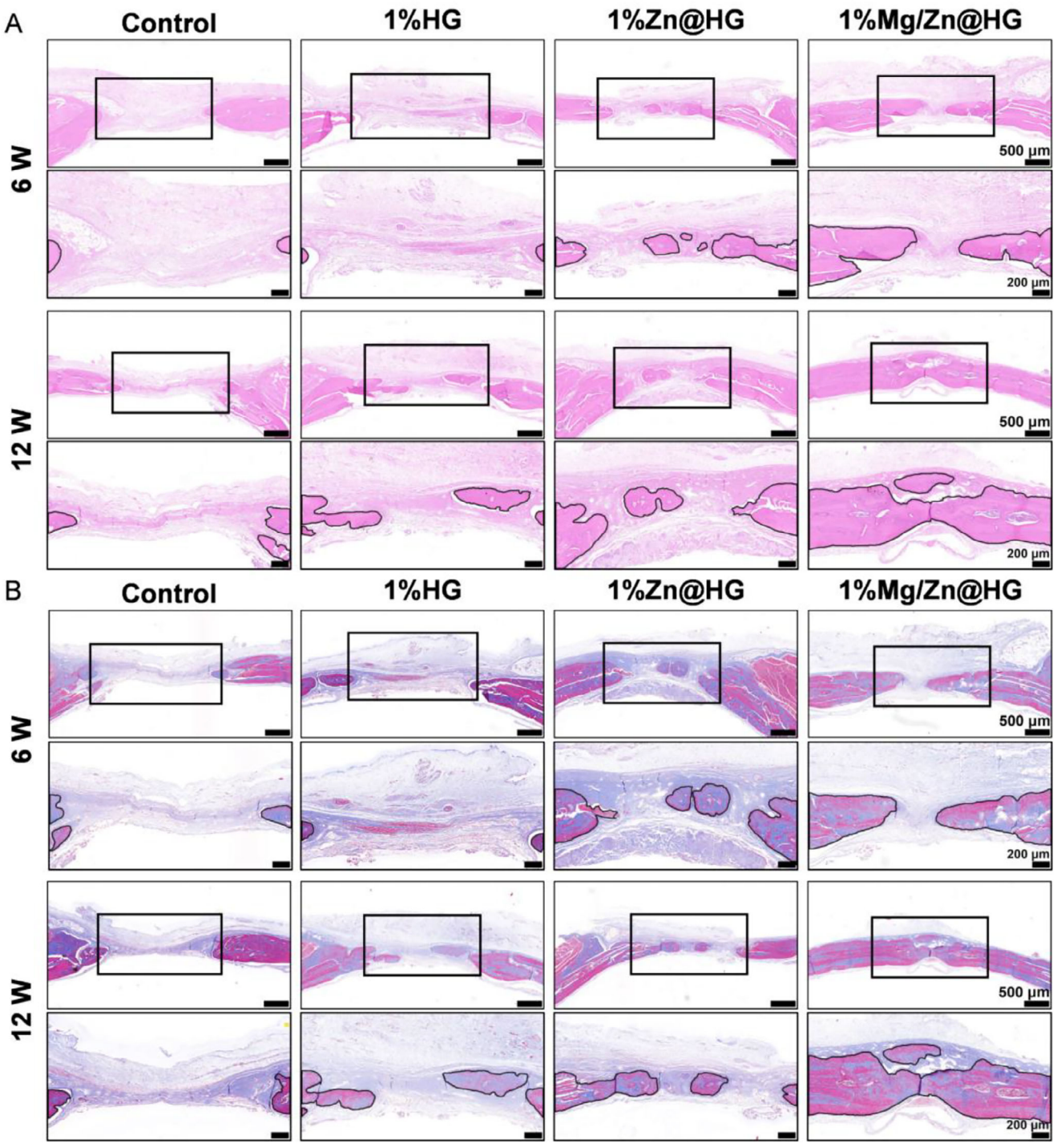

Figure 8. A) H&E and B) Masson staining of bone formation after 6 and 12 weeks of composite hydrogel scaffold implantation. The black circle indicates new bone. Scale bars are 500 and 200 μm, respectively.

3. Conclusion

This study successfully synthesized zinc-doped and magnesium/zinc co-doped HAp via a hydrothermal method, achieving uniform particle sizes between 5–10 μm, and demonstrating excellent biocompatibility and controllable microstructures. The SEM and EDS analyses confirmed the uniform distribution of Zn and Mg elements within the HAp powder, indicating successful doping. The XRD and FT-IR analyses showed that the synthesized HAp maintained a well-preserved crystalline structure, with magnesium and zinc doping significantly influencing its crystallinity and lattice parameters, promoting a transition

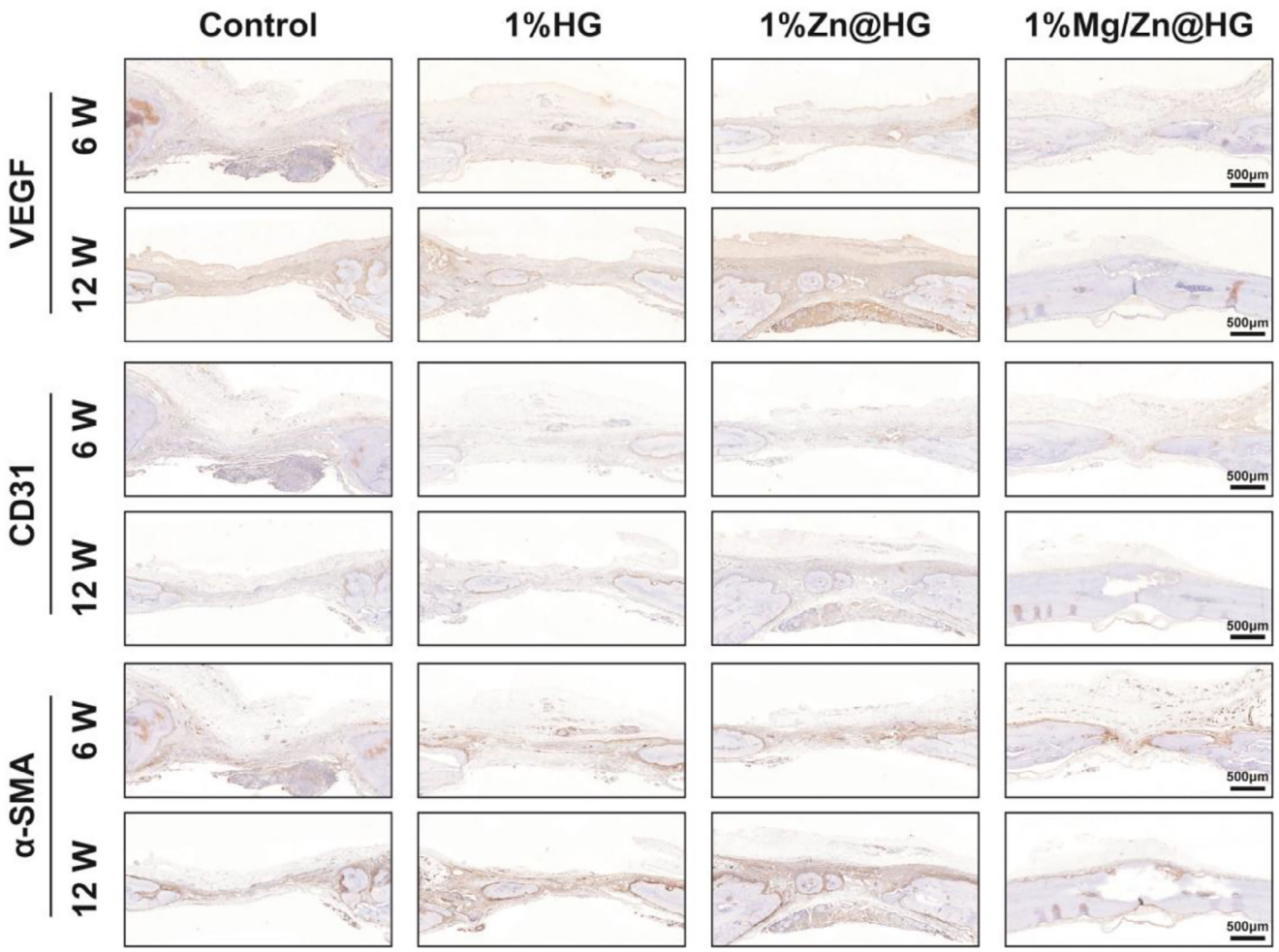

Figure 9. VEGF, CD31, α-SMA staining of bone formation after 6 and 12 weeks of composite hydrogel scaffold implantation. Scale bars are 500 μm.

toward a more spherical morphology. The synthesis and characterization of GelMA revealed its excellent biocompatibility and light-crosslinking properties, providing an ideal foundation for constructing biomaterial scaffolds. The resulting hydrogels from the HAp-GelMA composite exhibited good injectability and mechanical properties, highlighting their potential in biomedical applications to effectively support bone defect repair.

In vitro experiments, the results demonstrated that all composite hydrogel scaffolds possessed significant bioactivity with very low cytotoxicity, ensuring their safety for in vivo applications. Angiogenesis is crucial for bone regeneration, and experimental results indicated that the Zn/Mg dual-doped composite hydrogel scaffolds significantly enhanced the migration and tube formation of HUVECs, likely by promoting endothelial cell activity to facilitate vascularization, thereby supporting bone tissue repair. Additionally, in vitro osteogenic evaluations, the results showed that the Zn/Mg dual-doped composite hydrogel scaffolds effectively promoted rBMSCs osteogenic differentiation. In vivo studies, it was further revealed that these scaffolds exhibited significantly superior bone healing rates, bone density, and new bone mineralization compared to the control group, underscoring their exceptional performance in bone healing and enhancement of vascularization in defect areas. Overall, this research provides new insights into the development of biomaterials for bone repair and demonstrates the application potential of Zn/Mg dual-doped HAp-GelMA hydrogels in bone regeneration.

4. Experimental Section

Materials: Calcium nitrate tetrahydrate [$Ca(NO_3)_2{\cdot}4H_2O$, AR], magnesium nitrate hexahydrate [$Mg(NO_3)_2{\cdot}6H_2O$, AR]zinc nitrate tetrahydrate [$Zn(NO_3)_2{\cdot}4H_2O$, AR], phosphoric acid dodecahydrate disodium hydrogen ($Na_2HPO_4{\cdot}12H_2O$, AR), nitric acid (HNO_3, AR), glutaraldehyde ($C_5H_8O_2$, AR), urea (CH_4N_2O, AR) and absolute ethanol (AR) were purchased from Chengdu Kelong Chemical Reagent Factory. 1,2,3,4,5,6-Cyclohexanehexacarboxylic acid monohydrate (H_6L; $C_{12}H_{12}O_{12}{\cdot}H_2O$, AR) was purchased from TCI (Shanghai) Development Co., Ltd. (MW = 366.24, Shanghai, China).

Synthesis of HAp and Elements-Doped HAp: In this study, several HAp powders were synthesized using a hydrothermal method, consistent with previous research.[21] To prepare Zn-doped HAp with a Zn/(Zn + Ca) molar ratio of 10% (denoted as Zn@HAp), $Ca(NO_3)_2$, $Zn(NO_3)_2$, and Na_2HPO_4 were sequentially added to 150 mL of deionized water, maintaining a molar ratio of (Ca + Zn)/P at 1.67. For the Mg/Zn co-doped HAp with Zn/(Zn + Mg + Ca) = 10% and Mg/(Zn + Mg + Ca) = 5% (denoted as Mg/Zn@HAp), $Ca(NO_3)_2$, $Zn(NO_3)_2$, $Mg(NO_3)_2$, and Na_2HPO_4 were

similarly added to 150 mL of deionized water, keeping the molar ratio of (Ca + Zn + Mg)/P at 1.67. The resulting solution was mixed under magnetic stirring until a stable milky emulsion formed, and then 10.83 M HNO_3 was slowly added to adjust the pH to ≈2.3. Once the pH stabilized and the solution became clear, a template agent (1 M H_6L) was added and fully dissolved. Following this, 0.56 M urea was introduced into the solution, and after complete dissolution, the mixture was transferred to a six-position hydrothermal reactor and maintained at 200 °C for 12 h. After the reaction, the temperature was allowed to cool to room temperature, and the final product was collected. The precipitate was centrifuged at 4000 rpm for 3 min and alternately washed with deionized water and anhydrous ethanol. Finally, the obtained precipitate was dried at 65 °C for 48 h, yielding Zn@HAp and Mg/Zn@HAp powder samples. Undoped HAp powder was prepared using the same method and denoted as HAp. The specific grouping is shown in Table S1 (Supporting Information).

Characterization of Elements-Doped HA: To observe the morphology of the synthesized HAp powders, energy-dispersive X-ray spectroscopy (EDS) and scanning electron microscopy (SEM) were employed to analyze the morphology, size, and elemental composition of HAp, Zn@HAp, and Mg/Zn@HAp. Specifically, a small amount of each powder group was picked with a toothpick and placed onto a conductive adhesive-coated SEM sample stage, and any unadhered powder was blown away using a nitrogen gas gun. The sample stage was then placed in a high-vacuum coater for 30 seconds of gold sputtering. SEM observations of the powder morphology and microstructure were conducted at an acceleration voltage of 20 kV. The particle size of each group of HAp powder was then detected by Image J. Additionally, to verify the incorporation of Mg and Zn ions in the HAp powders, EDS was used for elemental detection and distribution analysis.

The quantity of doping elements in the samples was determined by inductively coupled plasma atomic emission spectra (ICP-OES, Avio 500, PerkinElmer).

Fourier-transform infrared spectroscopy (FT-IR) was employed to analyze the functional groups present in each group of HAp powders. Each HAp sample was mixed with potassium bromide (KBr), ground, and pressed into transparent pellets. FT-IR measurements were taken in the range of 4000–500 cm^{-1} to analyze the absorption characteristics and identify the functional groups present in each HAp sample. Furthermore, X-ray diffraction (XRD) analysis was performed to determine the phase composition of each HAp group, and standard cards were used to confirm the successful synthesis of HAp.

Preparation of Element-Doped HAp-GelMA Composite Hydrogel: Each group of HAp powders was added to a 10 wt.% GelMA prepolymer solution (containing 0.5 wt.% LAP) at concentrations of 0.5%, 1%, and 2 wt.%. The powders were uniformly dispersed in GelMA through magnetic stirring, resulting in composite hydrogel pre-solutions named 0.5%HG, 0.5%Zn@HG, 0.5%Mg/Zn@HG, 1%HG, 1%Zn@HG, 1%Mg/Zn@HG, 2%HG, 2%Zn@HG, and 2%Mg/Zn@HG. A volume of 200 µL from each group was transferred to a polytetrafluoroethylene cylindrical mold and cured for 30 s under 405 nm UV light before demolding for subsequent experiments. The specific grouping is shown in Table S2 (Supporting Information).

Characterization of Composite Hydrogel: To evaluate the injectability and photopolymerization properties of the composite hydrogels, 2%Mg/Zn@HG was used as an example. The uncured pre-solution was drawn into a syringe and extruded at room temperature to assess injectability. The pre-solution was then transferred to a round-bottom glass bottle, tilted, and exposed to 405 nm blue-violet light for 10s to observe curing and evaluate photopolymerization performance.

In order to observe the composite hydrogel scaffolds, the pre-polymer solutions of each group were added to a 24-well plate and exposed to blue-violet light with a wavelength of 405 nm for 10 s to photopolymerize the composite hydrogels, followed by taking photographs.

To observe the cross-sectional morphology and microstructure of the composite hydrogels as well as elemental distribution, the hydrogel scaffolds were placed in liquid nitrogen and fractured. The fractured surfaces were mounted face-up on an electron microscope sample stage with conductive adhesive and coated with gold for 60 s in a high-vacuum coater. The morphology and microstructure of the hydrogels were observed using SEM equipped with EDS at an acceleration voltage of 20 kV, followed by elemental detection and distribution analysis.

Fourier-transform infrared spectroscopy (FT-IR) was employed to analyze the functional groups present in each group of hydrogel scaffolds. Each sample was mixed with potassium bromide (KBr), ground, and pressed into transparent pellets. FT-IR measurements were taken in the range of 4000–500 cm^{-1} to analyze the absorption characteristics and identify the functional groups present in each HAp sample.

Absolute ethanol cannot dissolve the composite hydrogel and does not cause shrinkage or swelling of the hydrogel, making it suitable as a liquid for measuring the porosity of the composite hydrogel. The lyophilized composite hydrogels from each group were weighed and recorded as M_1, and the volume of each hydrogel was measured as V_{sample}. The hydrogels were then placed in EP tubes, and a certain amount of ethanol was added. After soaking for 24 h, the hydrogels were removed and gently wiped to remove excess ethanol from the surface, followed by weighing and recording as M_2. The density of Absolute ethanol ($\rho_{ethanol}$) is known to be 0.789 g cm^{-3}. The porosity (P) of the composite hydrogel was then calculated using the formula:

$$P = \frac{M_2 - M_1}{\rho ethanol \times Vsample} \times 100\% \quad (1)$$

Next, the swelling performance of the composite hydrogels was assessed. After freeze-drying, each hydrogel was weighed (denoted as M_d). The hydrogels were then immersed in PBS at 37 °C for 24 h to reach swelling equilibrium. After removing the samples, residual moisture on the surface was absorbed with filter paper, and the weight was recorded (denoted as M_w). The swelling ratio was calculated using the formula:

$$\text{Swelling ratio} = \frac{M_w}{M_d} \times 100\% \quad (2)$$

Subsequently, the rheological properties of the composite hydrogels were evaluated using a rotational rheometer at 25 °C, applying a fixed strain of 1% and performing frequency scans from 0.1 to 100 rad s^{-1} to determine the storage modulus (G') and loss modulus (G“”).

To assess the mechanical properties of the composite hydrogels, a universal testing machine was used for compression tests. The diameter and height of each sample were measured, and uniaxial compression tests were conducted at a rate of 1 mm min^{-1} at room temperature. The strain and stress were calculated using Equations (1) and (2), respectively, and stress–strain curves were plotted using Origin, with the slope of the 0%–20% stress–strain curve calculated to determine the compressive modulus.

$$\text{Strain} = \frac{\text{Displacement}}{\text{Original Height}} \times 100\% \quad (3)$$

$$\text{Stress} = \frac{\text{Load}}{\text{Cross} - \text{Sectional Area}} \times 100\% \quad (4)$$

To evaluate the in vitro degradation performance of the composite hydrogels, the hydrogels were freeze-dried and weighed (denoted as M_0). Each 10 mg of freeze-dried composite hydrogel was immersed in 1 mL of PBS at 37 °C. Samples were collected and freeze-dried on days 3, 7, 14, and 21, with weights recorded as M_t. The degradation rate of the hydrogel scaffold was calculated using the formula:

$$\text{Degradation rate} = \frac{M_0 - M_t}{M_0} \times 100\% \quad (5)$$

Finally, the release rate of Zn and Mg elements was measured using ICP-AES. Each group of composite hydrogels was freeze-dried and weighed, then immersed in PBS to achieve a concentration of 10 mg mL^{-1}. The samples were placed in a constant temperature shaking incubator at

37 °C and 90 rpm for 1, 2, 3, 7, and 14 days. At each time point, the supernatant was collected and replaced with an equal volume of fresh PBS, continuing the shaking process until the release was complete.

Isolation of Primary Rat Bone Marrow Mesenchymal Stem Cells (rBMSCs): Male SD rats aged 3–4 weeks were euthanized using cervical dislocation. The rats were immersed in a 75% ethanol solution for 30 min, and then transferred to a biological safety cabinet. Using sterilized surgical scissors and tweezers, the skin and muscle tissues of the hind legs were separated, and the bilateral hip joints were severed to extract the lower limbs. Residual tendons and muscles were removed to obtain the femur and tibia, which were rinsed in sterile PBS to remove blood. The ends of the femur and tibia were cut off to expose the marrow cavity, and a 1 mL syringe was used to flush the cavity with α-MEM culture medium containing 10% fetal bovine serum and 1% penicillin-streptomycin until the bone marrow was white. The wash solution was filtered through a 70 µm mesh to remove muscle and bone debris, yielding a single-cell suspension. This suspension was placed in a culture dish and incubated at 37 °C with 5% CO_2. After 3 days, a partial medium change was performed, followed by a complete medium change after an additional 2 days. Thereafter, the medium was replaced every 3 days until the cell confluence reached 90%, at which point the cells were passaged. To ensure cell viability and differentiation potential, cells from passages 3 to 5 were selected.

Extraction of Leachates from Composite Hydrogel Scaffolds: A total of 200 µL of the prepolymer solution from 1% HG, 1% Zn@HG, and 1% Mg/Zn@HG composite hydrogels was transferred to sterilized polytetrafluoroethylene cylindrical molds and cross-linked under 405 nm blue-violet light for 10 s before demolding. Subsequently, 2 mL of complete α-MEM or DMEM was added, and then incubated at 37 °C with 5% CO_2 for 24 h, collected as conditioned media.

Biocompatibility Assessment of Composite Hydrogel Scaffolds: The cell proliferation activity of the composite hydrogel scaffolds was evaluated using the CCK-8 method. The HAp microparticles synthesized in Section 2 were placed in EP tubes and sterilized by autoclaving. A 10 wt.% GelMA prepolymer solution (containing 0.5 wt.% LAP) was filtered for sterilization. The HAp microparticles were uniformly dispersed in the GelMA prepolymer solution at concentrations of 0.5%, 1%, and 2 wt.%. A total of 100 µL of each composite hydrogel prepolymer solution was evenly spread over the bottom of a 24-well plate and cross-linked under UV light at 405 nm for 30 s to obtain the corresponding hydrogels. A control group without hydrogel was also established.

HUVEC (purchased from ATCC) were carefully resuspended at a density of 2×10^4 cells/well and evenly seeded in a six-well plate, co-cultured with the hydrogels or control plates. The DMEM complete medium (containing 10% fetal bovine serum and 1% penicillin-streptomycin) was changed every 2 days. HUVECs were maintained in DMEM + 10% FBS (rather than specialized endothelial growth medium) in order to minimize the influence of exogenous angiogenic factors; this allowed us to attribute changes in cell behavior to the hydrogel treatments. Primary rBMSCs were seeded in another 24-well plate at the same density and co-cultured with the hydrogels or control plates, with the α-MEM complete medium replaced every 2 days.

On days 1, 3, and 5, rBMSCs and HUVEC co-culture plates were analyzed by adding CCK-8 reagent to each well, followed by incubation at 37 °C in the dark for 60 min. A total of 100 µL of the CCK-8 solution was then transferred to a 96-well plate, and the absorbance of each well was measured at 450 nm using a microplate reader for data collection and further analysis.

Subsequently, the cytotoxicity of the composite hydrogels was assessed using a live/dead cell staining method. A total of 100 µL of the 1% HG, 1% Zn@HG, and 1% Mg/Zn@HG prepolymer solutions were added to a confocal dish and cross-linked under 405 nm blue-violet light for 10 s. Primary rBMSCs and HUVECs were evenly seeded at a density of 5×10^4 cells well^{-1} in the confocal dish and cultured overnight to promote attachment. The medium was then replaced with a conditioned medium, changing the leachate daily. After 3 days of co-culture, the medium was aspirated, and the dishes were gently washed with PBS. An appropriate amount of Calcein-AM/PI staining solution was added, followed by incubation at 37 °C in the dark for 20 min. After aspirating the staining solution, the dishes were washed with PBS again and observed under a laser confocal microscope. Live cells stained with Calcein-AM (green) were detected using 488 nm excitation light, while dead cells stained with PI (red) were observed using 555 nm excitation light.

In Vitro Assessment of Vascular Formation Induced by Composite Hydrogel Scaffolds: The effect of the composite hydrogel scaffolds on the migration ability of HUVECs was evaluated using a scratch assay. HUVECs were evenly seeded at a density of 2×10^5 cells well^{-1} in a 12-well plate and incubated at 37 °C with 5% CO_2 until the cell confluence reached 80%–90%. Using a sterile 200 µL pipette tip, a straight line scratch was made in the center of each well, ensuring a consistent width for the scratch. Subsequently, gently wash away the suspended cells with PBS. Replace the DMEM culture medium with the conditioned medium for each group, and renew the conditioned medium daily. Images of the scratched area were taken at 0, 24, and 48 h using an inverted microscope, and the changes in scratch width were analyzed using ImageJ to quantify cell migration, the wound area at each time point was quantified and expressed as a percentage of the initial (0 h) wound area for the same well.

Subsequently, the effect of the composite hydrogel scaffolds on the tube formation ability of HUVECs was assessed through a tube formation assay. A 96-well plate, pipette tips, and centrifuge tubes were pre-chilled in a refrigerator at 4 °C. The matrix gel was mixed with a complete DMEM medium in equal volumes, and 50 µL of the diluted matrix gel was added to the pre-cooled 96-well plate. After gently mixing, the plate was incubated in a cell culture incubator for 30 min to allow the liquid matrix gel to solidify. Healthy HUVECs were digested and collected, followed by centrifugation at 1500 rpm for 5 min to discard the supernatant. The cells were then resuspended in conditioned media to a density of 2×10^5 cells mL^{-1}, and 100 µL of the cell suspension was added to each well containing the solidified matrix gel. The plate was incubated in the cell culture incubator, and after 4 h, the tube formation of HUVECs was observed and recorded using an inverted microscope. The number of formed tubes was quantified and analyzed using ImageJ software.

Detection of Angiogenesis-Related Gene Expression in Composite Hydrogel Scaffolds: The expression of angiogenesis-related genes was assessed using real-time quantitative reverse transcription polymerase chain reaction (RT-qPCR). HUVECs were evenly seeded at a density of 1×10^5 cells well^{-1} in a 6-well plate and incubated overnight for cell adhesion. After replacing the complete DMEM medium with the respective conditioned media, the media were changed every two days. Following a 5 days culture period, the expression of angiogenesis-related genes (HIF-1α and VEGF) was analyzed using the Bio-Rad RT-qPCR system, with GAPDH serving as the reference gene. The primer sequences used in the analysis are summarized in Table S3 (Supporting Information).

Additionally, the expression of angiogenesis-related proteins was evaluated through Western blotting (WB). HUVECs were seeded at the same density of 1×10^5 cells well^{-1} in a 6-well plate and allowed to adhere overnight. The complete DMEM medium was replaced with conditioned media, and the media were changed every two days. After 5 days of culture, protein extraction was performed for subsequent analysis. HUVECs were lysed on ice for 30 min in 200 µL of RIPA lysis buffer. After that, the samples were centrifuged at 14000 × g at 4 °C for 15 min. The supernatants were collected and the protein concentrations were measured by BCA protein assay kit (Beyotime, China). The samples were separated by Precast Protein Plus Gel (36250ES10, YEASEN, China) and then transferred onto a polyvinylidene difluoride (PVDF) membrane. The membranes were blocked in TBST, the solution with 5% BSA (Beyotime, China), and then the membranes were incubated overnight with anti-HIF-1α (1:1000, Proteintech, China), anti-VEGF (1:1000, Proteintech, China) and anti-GAPDH (1:1000, Proteintech, China) antibodies. Then the membranes were incubated with an HRP-conjugated secondary antibody. The band signals were detected by a chemiluminescence imaging system (Tanon, China).

In Vitro Osteogenic Evaluation of Composite Hydrogel Scaffolds: The 1%HG, 1%Zn@HG, and 1%Mg/Zn@HG composite hydrogel scaffolds were placed in sterilized centrifuge tubes, and 2 mL of osteogenic induction medium (α-MEM complete medium supplemented with 100 nM dexamethasone, 5 mM β-glycerophosphate, and 50 µg mL^{-1} ascorbic acid) was added. The scaffolds were incubated at 37 °C for 24 h to extract the

osteogenic induction medium. Primary rBMSCs were digested and centrifuged, then resuspended in α-MEM complete medium to form a single-cell suspension. The cells were seeded at a density of 1×10^5 cells well^{-1} in a 6-well plate and incubated overnight at 37 °C in a 5% CO_2 environment. The α-MEM complete medium of each scaffold group was replaced with the osteogenic induction medium every 2 days.

After 7 and 14 days of osteogenic induction, the medium was discarded, and the wells were washed gently three times with PBS. Then, 4% paraformaldehyde was added for 30 min to fix the cells, which were then washed again three times with ultrapure water. Alkaline phosphatase (ALP) staining solution (BCIP/NBT) was prepared according to the manufacturer's instructions, and 500 µL of the staining solution was added to each well. The plates were incubated in the dark at room temperature for 30 min. After discarding the staining solution, the cells were washed gently with ultrapure water 2–3 times, and the staining was observed and photographed under a microscope.

Additionally, ALP activity was measured to assess the osteogenic effect of the composite hydrogel scaffolds on rBMSCs. After 7 and 14 days of osteogenic induction, the medium was again discarded, and the wells were washed three times with PBS. A total of 500 µL of 0.5% (v/v) Triton X-100 solution was added to each well, and the plates were incubated at 37 °C for 90 min to obtain cell lysates. The protein concentration of each group was measured using a BCA assay kit to standardize the ALP activity. ALP activity was assessed using an ALP detection kit, with the OD at 405 nm measured and normalized to the corresponding total protein amount to yield final ALP activity results.

Finally, calcified nodules were detected using Alizarin Red S (ARS) staining. After 21 days of osteogenic induction, the medium was discarded, and the wells were washed three times with PBS. The cells were fixed with 4% paraformaldehyde for 30 min, then washed three times with ultrapure water. Each well received 500 µL of 2% Alizarin Red S staining solution, and the plates were incubated in the dark at room temperature for 30 min. The staining solution was removed, and the cells were washed again with ultrapure water 2–3 times. The formation of calcified nodules was observed and photographed under a microscope. Following staining, the wells were destained by adding 500 µL of 10% cetylpyridinium chloride solution at 37 °C for 15 min. The OD was measured at 562 nm using a microplate reader, and the data were collected for semi-quantitative analysis.

In Vitro Evaluation of Osteogenic-Related Gene Expression in Composite Hydrogel Scaffolds: The expression of osteogenic-related genes was assessed using RT-qPCR. rBMSCs were seeded at a density of 1×10^5 cells well^{-1} in a 6-well plate and incubated overnight to allow cell adhesion. The α-MEM complete medium was then replaced with the respective osteogenic induction medium every two days for a total of 14 days.

After the incubation period, the expression levels of osteogenic-related genes, including osteocalcin (OCN), osteopontin (OPN), and collagen type I (COL I), were measured using the RT-qPCR system. β-actin was used as an internal control for normalization. The primer sequences used in the analysis are summarized in Table S3 (Supporting Information).

The expression levels of osteogenic-related proteins were evaluated through Western blotting. rBMSCs were seeded at the same density of 1×10^5 cells well^{-1} in a 6-well plate and allowed to adhere overnight. After replacing the medium with the osteogenic induction medium, the cells were cultured for 14 days, with medium changes every two days. Following the incubation, the proteins were extracted using the same method mentioned earlier, and the samples were prepared for Western blot analysis to determine the expression of osteogenic markers. The membranes of BMSCs were incubated overnight with anti-COL1 (1:500, Proteintech, China), anti-OPN (1:1000, Proteintech, China) and anti-GAPDH (1:1000, Proteintech, China) antibodies. Then the membranes were incubated with an HRP-conjugated secondary antibody. The band signals were detected by a chemiluminescence imaging system (Tanon, China).

In Vivo Experiments–Animal Surgical Procedure for In Vivo Studies: In this experiment, a total of 24 male Sprague-Dawley (SD) rats, aged 8 weeks and weighing between 200 and 250 g, were randomly divided into four groups: Control, 1%HG, 1%Zn@HG, and 1%Mg/Zn@HG. For anesthesia, a solution of 2% sodium pentobarbital was administered via intraperitoneal injection at a dosage of 0.2 mL/100 g body weight. Once anesthesia was confirmed, the surgical area was shaved using clippers, and preoperative disinfection was performed with iodophor and alcohol. A sterile drape was placed over the area. A longitudinal incision ≈2–3 cm long was made along the midline of the skull, and the skin and subcutaneous tissue were dissected layer by layer until the periosteum was reached. The periosteum was then peeled back to expose the skull. Using a 5 mm diameter trephine, a full-thickness bone defect model was created on one side of the skull. After penetrating the skull completely, the bone fragment was carefully removed; the same procedure was performed on the contralateral side. Each hydrogel precursor solution was then injected into the defect area to fill it adequately. The area was exposed to 405 nm blue-violet light for 10 s to cure the hydrogel. The subcutaneous tissue was sutured layer by layer, followed by intermittent suturing of the skin. During the surgery, the vital signs of the rats were closely monitored. After surgery, the rats were housed in separate cages and received daily intramuscular injections of veterinary penicillin at a dosage of 20000 units kg^{-1} for three consecutive days. At 6 and 12 weeks post-surgery, three rats from each group were overdosed with anesthetics and euthanized to collect cranial bone specimens.

Micro-CT and Histological Evaluations: The collected specimens were fixed in 4% paraformaldehyde for 24 h, followed by washing with running water. Subsequently, Micro-CT scans were performed to evaluate bone regeneration across the groups. The cranial specimens were then transferred to EDTA decalcifying solution, with the solution being changed daily until the specimens could be easily penetrated with a syringe needle. After decalcification, the specimens were embedded in paraffin and sliced into 5 µm sections. Histological evaluations were conducted using H&E staining and Masson staining to assess the performance of the hydrogel scaffolds in repairing cranial bone defects. The sections were examined by pathological tissue section scanner (Pannoramic MIDI II, 3DHIETECH, Hungary).

Immunohistochemistry: Tissue sections (4 µm thick) were deparaffinized, rehydrated, and subjected to antigen retrieval using sodium citrate buffer (pH 6.0). Endogenous peroxidase activity was quenched with 3% H_2O_2, followed by blocking with 5% BSA. Primary antibodies were incubated overnight at 4 °C, including anti-CD31, anti-VEGF, and anti-α-SMA. HRP-conjugated secondary antibodies and DAB substrate were used for visualization. The sections were examined by pathological tissue section scanner (Pannoramic MIDI II, 3DHIETECH, Hungary).

Statistical Analysis: In this study, all experimental results are expressed as mean ± standard deviation. Statistical graphs were generated using GraphPad Prism 8.0.2 and Origin, and significance differences were evaluated using t-tests and one-way ANOVA. A p-value of less than 0.05 indicates a significant difference between groups (where * represents $p < 0.05$, ** represents $p < 0.01$, and *** represents $p < 0.001$).

Ethical Approval and Consent to Participate: The animal surgical procedures involved in this study follow the recommendations of the Institutional Animal Care and Use Committee (IACUC) of Shanghai Jiao Tong University, the animal protocol number is A2024228-001.

Supporting Information

Supporting Information is available from the Wiley Online Library or from the author.

Acknowledgements

L.Q. and T.Z. contributed equally to this work. The authors would like to acknowledge the creation of Figure 1 which was generated using biorender.com. This work was supported by the National Key R&D Program of China (2022YFA1207500); China Postdoctoral Science Foundation (2022M722121).

Conflict of Interest

The authors declare no conflict of interest.

Data Availability Statement

The data that support the findings of this study are available from the corresponding author upon reasonable request.

Keywords

angiogenesis, bone regeneration, GelMA, magnesium/zinc co-doping HAp, osteogenic

Received: February 24, 2025
Revised: July 5, 2025
Published online:

[1] J. H. Zeng, S. W. Liu, L. Xiong, P. Qiu, L. H. Ding, S. L. Xiong, J. T. Li, X. G. Liao, Z. M. Tang, *J. Orthop. Surg. Res.* **2018**, *13*, 33.
[2] M. Sadat-Shojai, M. T. Khorasani, A. Jamshidi, *Chem. Eng. J.* **2016**, *289*, 38.
[3] R. Dimitriou, G. I. Mataliotakis, A. G. Angoules, N. K. Kanakaris, P. V. Giannoudis, *Injury* **2011**, *42*, S3.
[4] S. R. Nodzo, N. B. Kaplan, D. W. Hohman, C. A. Ritter, *Int Orthop.* **2014**, *38*, 1199.
[5] J. Li, W. Zhi, T. Xu, F. Shi, K. Duan, J. Wang, Y. Mu, J. Weng, *Regener. Biomater.* **2016**, *3*, 285.
[6] P. X. Ma, *Adv. Drug Delivery Rev.* **2008**, *60*, 184.
[7] a) J. Wang, Y. Wu, G. Li, F. Zhou, X. Wu, M. Wang, X. Liu, H. Tang, L. Bai, Z. Geng, P. Song, Z. Shi, X. Ren, J. Su, *Adv. Mater.* **2024**, *36*, 2309875; b) X. Ren, J. Wang, Y. Wu, Y. Zhang, J. Zhang, L. Bai, J. Liu, G. Li, P. Song, Z. Shi, J. Su, *J. Mater. Sci. Technol.* **2024**, *188*, 84.
[8] M. A. Saghiri, J. Vakhnovetsky, A. Vakhnovetsky, M. Ghobrial, D. Nath, S. M. Morgano, *J. Trace Elem. Med. Biol.* **2022**, *71*, 126932.
[9] R. J. M. Lynch, *Int. Dent. J.* **2011**, *61*, 46.
[10] a) A. S. Tiffany, D. L. Gray, T. J. Woods, K. Subedi, B. A. C. Harley, *Acta Biomater.* **2019**, *93*, 86; b) X. Fu, Y. Li, T. Huang, Z. Yu, K. Ma, M. Yang, Q. Liu, H. Pan, H. Wang, J. Wang, M. Guan, *Adv. Sci.* **2018**, *5*, 1700755.
[11] a) M. Yamaguchi, M. N. Weitzmann, *Mol. Cell. Biochem.* **2011**, *355*, 179; b) K. Huo, X. Zhang, H. Wang, L. Zhao, X. Liu, P. K. Chu, *Biomaterials* **2013**, *34*, 3467.
[12] J. P. O'Connor, D. Kanjilal, M. Teitelbaum, S. S. Lin, J. A. Cottrell, *Materials* **2020**, *13*, 2211.
[13] S. Wang, R. Gu, F. Wang, X. Zhao, F. Yang, Y. Xu, F. Yan, Y. Zhu, D. Xia, Y. Liu, *Mater. Today Bio.* **2022**, *13*, 100202.
[14] a) A. Hartwig, *Mutat. Res. Fund. Mol. Mech. Mutagen.* **2001**, *475*, 113; b) N. E. Saris, E. Mervaala, H. Karppanen, J. A. Khawaja, A. Lewenstam, *Clin. Chim. Acta* **2000**, *294*, 10727669.
[15] a) G. Stendig-Lindberg, W. Koeller, A. Bauer, P. M. Rob, *Eur. J. Intern. Med.* **2004**, *15*, 97; b) S. Bernick, G. F. Hungerford, *J. Dent. Res.* **1965**, *44*, 1317.
[16] J. A. Maier, D. Bernardini, Y. Rayssiguier, A. Mazur, *Biochimica et Biophysica Acta – Mole. Basis of Disease* **2004**, *1689*, 6.
[17] H. K. Kim, H. S. Han, K. S. Lee, D. H. Lee, J. W. Lee, H. Jeon, S. Y. Cho, H. J. Roh, Y. C. Kim, H. K. Seok, *J. Tissue Eng. Regener. Med.* **2017**, *11*, 2710.
[18] S. Yoshizawa, A. Brown, A. Barchowsky, C. Sfeir, *Acta Biomater.* **2014**, *10*, 2834.
[19] K. Yue, G. Trujillo-de Santiago, M. M. Alvarez, A. Tamayol, N. Annabi, A. Khademhosseini, *Biomaterials* **2015**, *73*, 254.
[20] a) I. Pepelanova, K. Kruppa, T. Scheper, A. Lavrentieva, *Bioengineering* **2018**, *5*, 55; b) C. M. Madl, S. C. Heilshorn, H. M. Blau, *Nature* **2018**, *557*, 335.
[21] H. Huang, L. Qiang, M. Fan, Y. Liu, A. Yang, D. Chang, J. Li, T. Sun, Y. Wang, R. Guo, H. Zhuang, X. Li, T. Guo, J. Wang, H. Tan, P. Zheng, J. Weng, *Bioact. Mater.* **2024**, *31*, 18.
[22] H. Kim, S. Mondal, S. Bharathiraja, P. Manivasagan, M. S. Moorthy, J. Oh, *Ceram. Int.* **2018**, *44*, 6062.
[23] D. Fan, S. Wei, M. Ma, Z. Chen, B. Li, H. Xie, *Phys. Chem. Miner.* **2014**, *41*, 85.
[24] Y. Sun, G. Guo, Z. Wang, H. Guo, *Ceram. Int.* **2006**, *32*, 951.
[25] a) S. Bupphathong, C. Quiroz, W. Huang, P. F. Chung, H. Y. Tao, C. H. Lin, *Pharmaceuticals* **2022**, *15*, 171; b) J. J. Su, C. H. Lin, H. Chen, S. Y. Lee, Y. M. Lin, *Polymers* **2021**, *13*, 2354; c) J. J.-M. Su, C.-H. Lin, H. Chen, S.-Y. Lee, Y.-M. Lin, *Polymers* **2021**, *13*, 2354; d) S. Kwon, S. S. Lee, A. Sivashanmugam, J. Kwon, S. H. L. Kim, M. Y. Noh, S. K. Kwon, R. Jayakumar, N. S. Hwang, *Polymers* **2018**, *10*, 914.
[26] J. Wang, X. Wang, Z. Liang, W. Lan, Y. Wei, Y. Hu, L. Wang, Q. Lei, D. Huang, *Front. Bioeng. Biotechnol.* **2023**, *11*, 1219460.
[27] S. H. Oh, D. B. An, T. H. Kim, J. H. Lee, *Acta Biomater.* **2016**, *35*, 23.
[28] a) P. F. Guan, Y. L. Ji, X. C. Kang, W. L. Liu, Q. F. Yang, S. C. Liu, Y. Y. Lin, Z. Y. Zhang, J. J. Li, Y. Zhang, C. Liu, L. Fan, Y. J. Sun, *ACS Appl. Mater. Interfaces* **2023**, *15*, 8986; b) N. Huebsch, P. R. Arany, A. S. Mao, D. Shvartsman, O. A. Ali, S. A. Bencherif, J. Rivera-Feliciano, D. J. Mooney, *Nat. Mater.* **2010**, *9*, 518.
[29] T. Liu, M. Jin, Y. Zhang, W. Weng, T. Wang, H. Yang, L. Zhou, *Ceram. Int.* **2021**, *47*, 30929.
[30] a) P. Kolar, T. Gaber, C. Perka, G. N. Duda, F. Buttgereit, *Clin Orthop Relat Res.* **2011**, *469*, 3118; b) C. S. Bahney, R. L. Zondervan, P. Allison, A. Theologis, J. W. Ashley, J. Ahn, T. Miclau, R. S. Marcucio, K. D. Hankenson, *J. Orthop. Res.* **2019**, *37*, 35.
[31] A. Hoppe, N. S. Guldal, A. R. Boccaccini, *Biomaterials* **2011**, *32*, 2757.
[32] M. Salandova, I. A. J. van Hengel, I. Apachitei, A. A. Zadpoor, B. C. J. van der Eerden, L. E. Fratila-Apachitei, *Adv. Healthcare Mater.* **2021**, *10*, 2002254.
[33] a) B. Conrad, L.-H. Han, F. Yang, *Tissue Eng., Part A* **2018**, *24*, 1631; b) X. Xue, Y. Hu, S. Wang, X. Chen, Y. Jiang, J. Su, *Bioact. Mater.* **2022**, *12*, 327.
[34] S. A. Sreenivasamurthy, F. F. Akhter, A. Akhter, Y. Su, D. Zhu, *Biomater. Adv.* **2022**, *139*, 213023.
[35] N. Di Maggio, A. Banfi, *Curr. Opin. Biotechnol.* **2022**, *76*, 102750.
[36] Z. Zhai, X. Qu, H. Li, K. Yang, P. Wan, L. Tan, Z. Ouyang, X. Liu, B. Tian, F. Xiao, W. Wang, C. Jiang, T. Tang, Q. Fan, A. Qin, K. Dai, *Biomaterials* **2014**, *35*, 6299.
[37] C. Li, W. Zhang, Y. Nie, X. Du, C. Huang, L. Li, J. Long, X. Wang, W. Tong, L. Qin, Y. Lai, *Adv. Mater.* **2024**, *36*, 2308875.
[38] F. L. Zhao, A. Gao, Q. Liao, Y. Y. Li, I. Ullah, Y. Zhao, X. X. Ren, L. P. Tong, X. Li, Y. D. Zheng, P. K. Chu, H. Y. Wang, *Adv. Funct. Mater.* **2024**, *34*, 2311812.
[39] Y. Li, W. Xiong, C. C. Zhang, B. Gao, H. F. Guan, H. Cheng, J. J. Fu, F. Li, *J. Biomed. Mater. Res. A* **2014**, *102*, 3939.
[40] J. W. Rasmussen, E. Martinez, P. Louka, D. G. Wingettt, *Expert. Opin. Drug. Del.* **2010**, *7*, 1063.
[41] L. Xu, R. Willumeit-Römer, B. J. C. Luthringer-Feyerabend, *Acta Biomater.* **2019**, *98*, 269.
[42] a) C. C. Hung, A. Chaya, K. Liu, K. Verdelis, C. Sfeir, *Acta Biomater.* **2019**, *98*, 246; b) Y. Li, J. K. Xu, J. Mi, X. He, Q. Pan, L. Z. Zheng, H. Y. Zu, Z. Y. Chen, B. Y. Dai, X. Li, Q. Q. Pang, L. Zou, L. B. Zhou, L. Huang, W. X. Tong, G. Li, L. Qin, *Biomaterials* **2021**, *275*, 120984.
[43] Y. Zhang, J. Xu, Y. C. Ruan, M. K. Yu, M. O'Laughlin, H. Wise, D. Chen, L. Tian, D. Shi, J. Wang, S. Chen, J. Q. Feng, D. H. Chow, X. Xie, L. Zheng, L. Huang, S. Huang, K. Leung, N. Lu, L. Zhao, H. Li, D. Zhao, X. Guo, K. Chan, F. Witte, H. C. Chan, Y. Zheng, L. Qin, *Nat. Med.* **2016**, *22*, 1160.